Zeitschrift: Helvetica Physica Acta

Band: 71 (1998)

Heft: Sep. 1

Vereinsnachrichten: Réunion de printemps de la Société Suisse de Physique = Frühjahrstagung der Schweizerischen Physikalischen Gesellschaft = Spring meeting of the Swiss Physical Society

Autor: [s.n.]

Réunion de Printemps de la Société Suisse de Physique

Frühjahrstagung der Schweizerischen Physikalischen Gesellschaft

Spring Meeting of the Swiss Physical Society

February 26 and 27, 1998

Bern, Switzerland

Helv. Phys. Acta 71, Separanda 1 (1998) S1 – S2
0018-0238/98/0100S1-02 $ 1.50+0.20/0

Helvetica Physica Acta

WRITING ELECTRONIC NANOFEATURES IN EPITAXIAL OXIDE HETEROSTRUCTURES

T. Tybell, C.H. Ahn, and J.-M. Triscone

DPMC, University of Geneva, 24 Quai Ernest Ansermet, 1211 Geneva 4, Switzerland

Using scanning probe microscopy and high quality epitaxial oxide heterostructures, we have written nonvolatile, reversible electronic nanofeatures in conducting oxides using a local ferroelectric field effect. The electronic structures were written in atomically smooth $Pb(Zr_{0.52}Ti_{0.48})O_3$ / $SrRuO_3$ heterostructures by controlling the local polarization field of the ferroelectric $Pb(Zr_{0.52}Ti_{0.48})O_3$ layer with an atomic force microscope, inducing a field effect in the 30Å thick $SrRuO_3$ layer. This novel doping technique permits one to write reversible and nonvolatile electronic structures without lithography or permanent electrical contacts. We also discuss writing and reading of ferroelectric domains with nanometer resolution over large areas of 2500 μm^2.

$Pb(Zr_xTi_{1-x})O_3$(PZT) is a perovskite material whose ferroelectric properties make it interesting for applications such as nonvolatile capacitor and ferroelectric field effect devices[1]. In this work, we have investigated the possibilities afforded by the nonvolatile polarization field of PZT to control locally the electronic properties on a submicrometer length scale via a local ferroelectric field effect.

To control the local ferroelectric domain structure, we have used a metallic AFM tip that is scanned in contact with the ferroelectric surface. To polarize a domain, an electric field is applied between the tip and a conducting ground plane that exceeds the coercive field of the material. To image domains, we then use the AFM to measure the piezoelectric response of the sample[2]. In this technique, a field smaller than the coercive field is applied to the sample. Because the sign of the piezoelectric deformation depends on the sign of the ferroelectric polarization, the piezoelectric response allows one to map the domain structure of the sample. To measure the piezoelectric response, a lock-in technique is used.

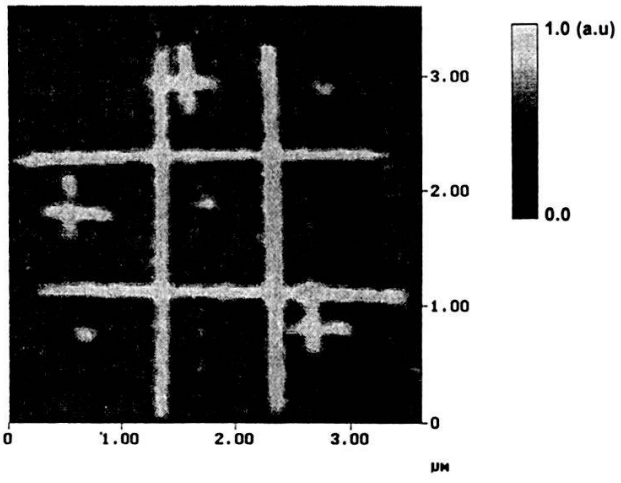

Figure 1. Piezoelectric image of written ferroelectric domains. 10 lines and 3 dots were written, all ~100nm wide, as determined from the FWHM values of the piezoelectric response.

For these experiments, we used ~1000Å thick $Pb(Zr_{0.2}Ti_{0.8})O_3$ films grown onto conducting Nb-doped $SrTiO_3$ substrates using RF-magnetron sputtering. The films are single crystalline and atomically smooth, showing an RMS roughness of typically 2Å over 5x5μm^2. With these films, large areas of up to 2500μm^2 have been successfully polarized in a homogenous fashion[3]. The high quality samples permit one to write arbitrary ferroelectric domain features without being influenced by topographic defects. One example is shown in Figure 1, where we have written ferroelectric domains in the form of ten lines and three dots on a homogeneous polarized background. The full widths at half maximum (FWHM) of the features are ~100nm.

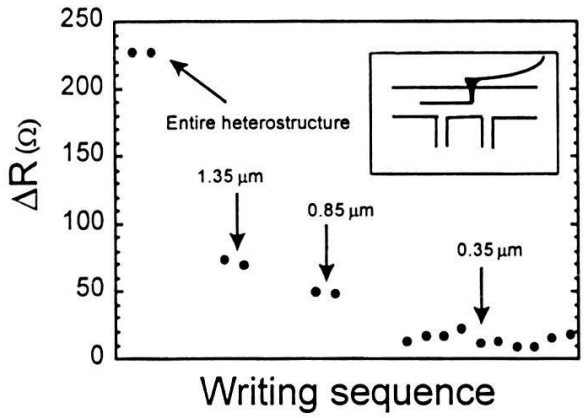

Figure 2. Change in resistance of the $SrRuO_3$ layer as a function of the linewidth of the written ferroelectric domains. The smallest electronic structures had widths of ~350nm.

Using this technique to locally control the ferroelectric polarization we have investigated the possibility to locally change the conductivity of an underlying metallic oxide in a ferroelectric / conducting oxide heterostructure via the ferroelectric field effect[4]. In this approach, the nonvolatile polarization field from the ferroelectric induces screening charges to flow in the underlying material, changing the local carrier concentration and hence the conductivity of the material. For this experiment we used 4000Å $Pb(Zr_{0.52}Ti_{0.48})O_3$ / 30Å $SrRuO_3$ heterostructures. Nonvolatile and reversible doping was obtained, with the smallest electronic structures having a linewidth of 350nm. In Figure 2, we show the change in resistance of the $SrRuO_3$ layer between the two polarization states of the PZT film for features of different linewidths. By polarizing the entire heterostructure, a 7% change in resistance was obtained, in good agreement with macroscopic measurements[1] that showed a 9% change in the resistivity. As the written linewidth was decreased the measured change in resistance decreased linearly with the written surface area, as expected. For the writing of the 0.35μm lines, we repeated the writing measurement 10 times. The average change in resistance between the two polarization states obtained was 14.9 Ω, with a standard deviation of 4.3 Ω.

In conclusion, we have explored the possibility of using a local probe to control the ferroelectric polarization over large areas with submicrometer resolution in high quality ferroelectric materials. This local control presents a new way to locally change the electronic structure of an underlying material in a reversible and nonvolatile manner. Using this technique, electronic structures as small as 350nm were reproducibly realized.

References:

1. C.H. Ahn, J.-M. Triscone, N. Archibald, M. Decroux, R.H. Hammond, T.H. Geballe, Ø. Fischer, and M. R. Beasley, Science **269**, 373 (1995); C.H. Ahn, R.H. Hammond, T.H. Geballe, M.R. Beasley, J.-M. Triscone, M. Decroux, and Ø. Fischer, L. Antognazza, and K. Char, Appl. Phys. Lett. **70**, 206 (1997).

2. P. Güthner and K. Dransfeld, Appl. Phys. Lett. **61**, 1137 (1992).

3. T. Tybell, C.H. Ahn, and J.-M. Triscone, to appear in Appl. Phys. Lett. 23/3/98.

4. C. H. Ahn, T. Tybell, L. Antognazza, K. Char, R. H. Hammond, M. R. Beasley, Ø. Fischer, and J.-M. Triscone, Science **276**, 1100 (1997); C. H. Ahn, T. Tybell, L. Antognazza, K. Char, R. H. Hammond, M. R. Beasley, Ø. Fischer, and J.-M. Triscone, to appear in Mat. Res. Soc. Symp. Proc.

Helv. Phys. Acta 71, Separanda 1 (1998) S3 – S4
0018-0238/98/0100S3-02 $ 1.50+0.20/0

Helvetica Physica Acta

Micromechanical thermal gravimetry performed on one single zeolite crystal

L. Scandella, J.-H. Fabian, C. v. Scala
Paul Scherrer Institut, Laboratory for Micro- and Nanostructures, 5232 Villigen PSI, Switzerland

R. Berger, H.P. Lang, Ch. Gerber, J.K. Gimzewski
IBM Zurich Research Division, Säumerstr. 4, 8803 Rüschlikon, Switzerland

E. Meyer
University of Basel, Institute for Physics, 4056 Basel, Switzerland

Thermal gravimetry (TG) is an analytical tool routinely used to study mass loss due to desorption or decomposition of material. Standard thermal analysis needs material quantities in the milligram range. Recently, micromechanical thermal gravimetry (MMTG) has been reported to perform TG analysis on nanogram and picogram samples [1]. For that purpose piezoresistive cantilevers used for atomic force microscopy (AFM) are operated as a tiny microbalance. The masses of such cantilevers are typically in the nanogram range and combine short response times and high sensitivities well beyond what is achievable with standard techniques [2]. However, mass changes can be sensed with a theoretical mass resolution in the femtogram realm. Recent experiments based on mass changes of cantilevers were reported for sensing humidity [3].

In this article thermo gravimetric experiments for investigation of picogram mass changes based on the desorption of molecules from on single zeolite crystal are presented.

A piezoresistive cantilever is mounted on a piezoelectric actuator and vibrated at its first resonance frequency. The resonance frequency can be monitored by measuring the change of resistivity of the piezoresistive layer upon cantilever bending. This is achieved using a Wheatstone bridge electrical circuit. For our MMTG applications, the applied bridge voltage is increased, resulting in an ohmic heating of the micromechanical piezoresistive layer. Temperatures up to several hundreds °C can be obtained.

A single zeolite crystal was glued to the apex of the cantilever (see Fig. 1). When the mass of the zeolite changes due to the adsorption or desorption of molecules, the resonance frequency decreases or increases, respectively.

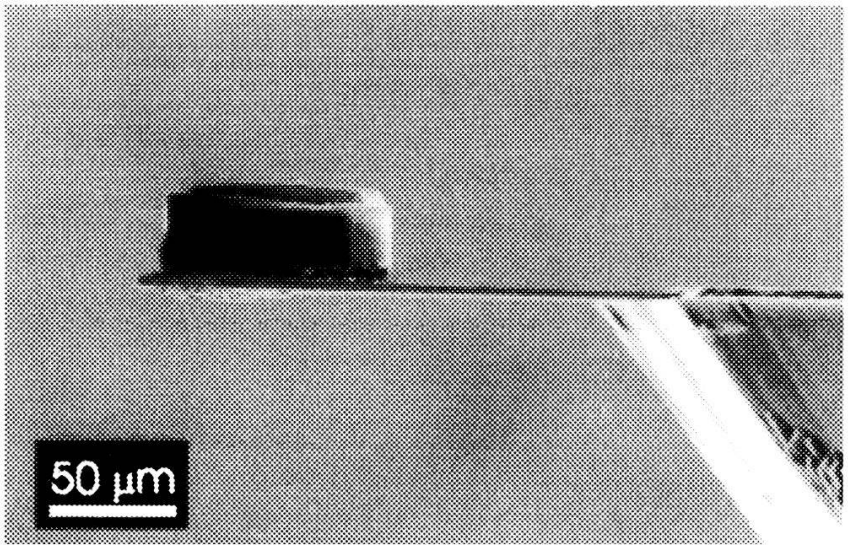

Fig. 1. A single zeolite crystal (ZSM-5) loaded with *p*-nitroaniline is attached to a piezoresistive cantilever [4]. The scanning electron micrograph shows a side view of the cantilever with the zeolite crystal.

MMTG of an individual zeolite crystal loaded with molecules was performed. ZSM-5 zeolite crystals with dimensions of approximately 40 μm x 25 μm x 80 μm were loaded with *p*-nitroaniline (PNA) via the gas phase [5].
The cantilever temperature was ramped from a temperature of 20°C up to 300°C. As can be seen in Fig. 2, the desorption of PNA molecules from the zeolite was observed to occurs at 200°C. The weight loss of about 9% due to the desorption, caused a resonance frequency shift of 2 kHz. The absolute mass loss was of a few nanograms. This weight loss of 9% corresponds to 4 molecules per unit cell. The MMTG curve is in good agreement with standard TG analysis [5].
In conclusion, we showed the possibility to perform thermal gravimetric analysis on a single zeolite micro crystal at picogram level.

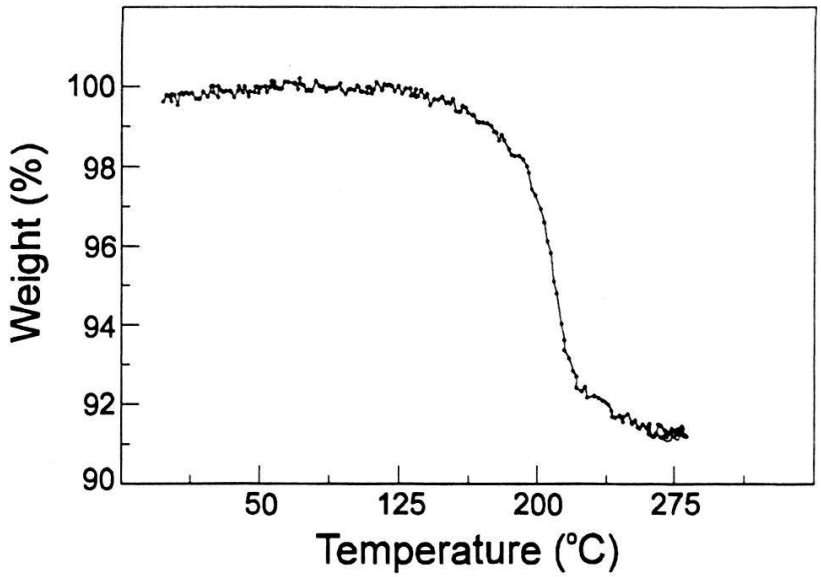

Fig. 2 Weight loss during desorption of *p*-nitroaniline molecules from one single ZSM-5 crystal measured by micromechanical thermal gravimetry.

We gratefully acknowledge J. C. Jansen and J.-H. Koegler for providing the ZSM-5 crystals. H.-J. Güntherodt is acknowledged for his support. This work is partially funded by Swiss Priority Program in Micro- and Nano System Technology (MINAST), No 7.04 NOSE.

References

[1] R. Berger, H.-P. Lang, Ch. Gerber, J. K. Gimzewski, E. Meyer, H.-J. Güntherodt and L. Scandella, submitted to Chem. Phys. Lett.
[2] J.K. Gimzewski, Ch. Gerber, E. Meyer and R.R. Schlittler, Chem. Phys. Lett. 217 (1994) 589.
[3] L. Scandella, G. Binder, T. Mezzacasa, J. Gobrecht, R. Berger, H.-P. Lang, Ch. Gerber, J.K. Gimzewski, J.H. Koegler and J.C. Jansen, Microporous Materials, in press.
[4] Park Scientific Instruments, 1171 Borregas Avenue, Sunnyvale, CA 94089.
[5] G. Binder, L. Scandella, J. Kritzenberger, J. Gobrecht, J.H. Koegler and R. Prins, Phys. Chem. B 101 (1997) 483.

Helv. Phys. Acta 71, Separanda 1 (1998) S5 – S6
0018-0238/98/0100S5-02 $ 1.50+0.20/0

Helvetica Physica Acta

Single-electron tunneling devices as a possible dc current standard

M. Furlan,[1,2] A. L. Eichenberger,[1] E. Käch,[1] B. Jeanneret,[1] and B. Jeckelmann[1]

[1]*Swiss Federal Office of Metrology, CH-3084 Wabern, Switzerland; and*
[2]*Solid State Physics Laboratory, ETHZ Hönggerberg, CH-8093 Zürich, Switzerland*

Control of the tunneling rate of single electrons is possible in systems of small tunnel junctions showing a Coulomb blockade. An external gate potential may be appropriately set to allow the transfer of an exactly given number of charges. With an rf drive at the gate, the dc current is consequently determined by the rf frequency.
We are currently investigating the feasibility of a new current standard, based on nanometer sized single-electron tunneling devices. A very brief status report is given, and first experimental results on the Coulomb blockade are presented.

Very small junction systems can exhibit quantum tunneling of individual charges q at very low temperatures T, where $k_B T$ is much smaller than the Coulomb energy $q^2/2C$. Typical junction capacitances are on the order of 0.1 fF. Single charge tunneling effects have attracted much attention in the last few years [1]. The basic picture of a single-electron tunneling (SET) device is two tunnel junctions, separating a small conductive island from the electrodes. Such SET transistors are currently the most sensitive electrometers, detecting charge at the level of $10^{-4}\ e/\mathrm{Hz}^{1/2}$.
Among many different application possibilities, SET devices are also under investigation as a very accurate current source (or detector) with metrological accuracy of better than 10^{-8}. In principle, an external gate potential which is coupled to the island controls the single charge transfer. With an external rf drive frequency f this leads to a dc current $I = nqf$, where q is the particle charge (e or $2e$ for electrons or Cooper pairs, respectively) and n a fixed integer number. The possibility to determine the current at high precision by correlated tunneling would close the "quantum metrology triangle", relating voltage, current and frequency (currently realized with the Josephson effect $V = (mh/2e)f$ and the Quantum Hall effect $V = (h/ie^2)I$, where m and i are integers). Promising candidates for dc current standards are multi-junction arrays ("turnstile", "single electron pump"): the outermost devices act as buffers towards the environment (i.e. connecting leads), whereas an increased number of devices in series increases the controllability of the electron phase through the array. The feasibility to attain an accuracy better than 10^{-8} has been predicted [2] already for arrays with 5...7 devices. The operation of a seven-junction pump with an error per pumped electron of 15×10^{-9} has recently been reported [3].
To achieve the desired performance, comprehensive studies on the devices (i.e. material, geometries, IV-characteristics, noise figure ...) have to be carried out. We have developed an experimental infrastructure to test and characterize SET devices at very low noise level. The devices themselves have to be well shielded against high energy photons which can excite the electrons above the Coulomb gap. To prevent triggering of the system by electromagnetic noise at temperatures above ~ 1 K (corresponding to ~ 20 GHz), the microwave-frequency radiation has to be heavily filtered. Our samples are enclosed by an electromagnetically tight copper cylinder. The problem of microwaves entering via the signal lines and their feed-through was successfully solved by introducing special thin coaxial cables (2 m per line) with strongly increasing losses at

the critical frequencies [4]. The low noise electronics (operating at room temperature) allow to measure IV-characteristics with both current or voltage bias, with a preamplifier resolution of 20 nV/Hz$^{1/2}$ or about 20 fA/Hz$^{1/2}$ (at 10 Hz), respectively.

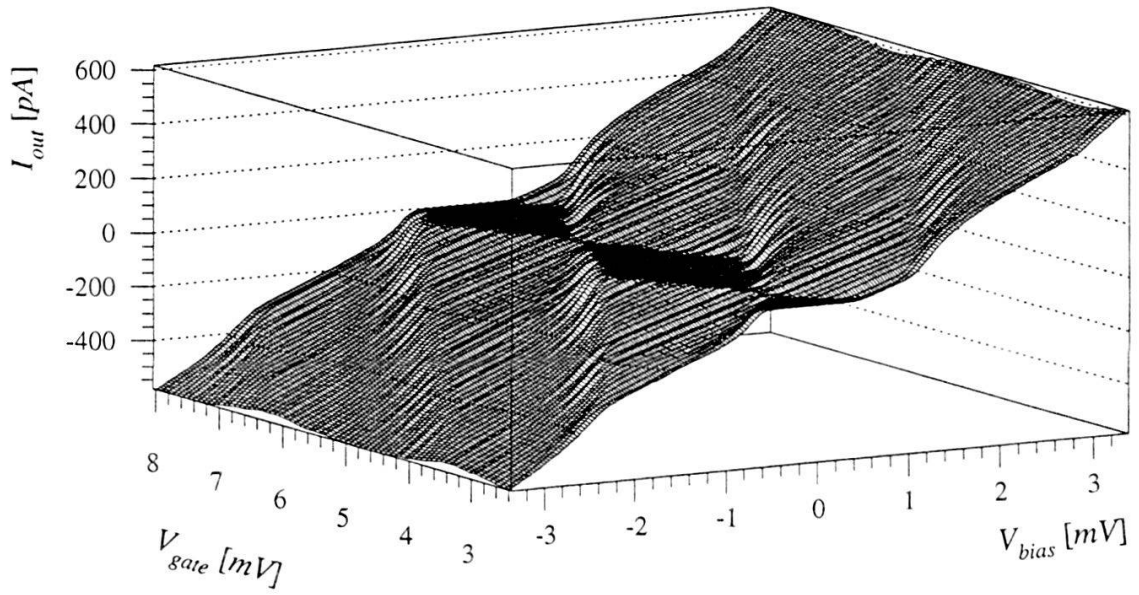

IV and modulation curves for different operating points. The Coulomb blockade is clearly developed (plateaus).

The figure shows the measured current through an Al/Al_2O_3/Al junction SET device [5] as a function of bias voltage V_{bias} and gate potential V_{gate}. The device is in the normalconducting state (1 T applied). At low bias voltage the Coulomb blockade is clearly observed (plateaus). The modulation period of the device current with V_{gate} corresponds to the variation of the total charge on the island by one elementary charge e. From the results the following device characteristics are derived: an asymptotic resistance R = 3.6 MΩ, a gate capacitance C_g = 57 aF and a total capacitance C_Σ = 145 aF.

Our devices show a noise performance with the characteristic $1/f$ contribution, which sets the dc sensitivity limits for the currently available SET devices. The fundamental limit would be given by shot noise. We have measured a noise density of typically $3...5\times10^{-4}$ e/Hz$^{1/2}$ (at 10 Hz). However, the usually observed two-level-fluctuator noise ("telegraph noise") was reduced to a negligible level after installation of the thorough screening precautions, proving the importance of a low-noise electromagnetic environment. Our efforts are currently towards the development of improved readout electronics with a sensitivity to extremely low currents and an increase of SET device bandwidth (above MHz in order to resolve single-electron events at a current level of nA).

[1] *Single Charge Tunneling, Coulomb Blockade Phenomena in Nanostructures*, edited by H. Grabert and M. H. Devoret (Plenum Press, New York, 1992).

[2] H. D. Jensen and J. M. Martinis, Phys. Rev. B **46**, 13407 (1992); H. Pothier, P. Lafarge, D. Esteve, C. Urbina, and M. H. Devoret, IEEE Trans. Instr. Meas. **42**, 324 (1993).

[3] M.W. Keller, J. M. Martinis, A. H. Steinbach and N. M. Zimmermann, IEEE Trans. Instr. Meas. **46**, 307 (1997).

[4] A. B. Zorin, Rev. Sci. Instrum. **66**, 4296 (1995).

[5] the devices were fabricated by the Physikalisch-Technische Bundesanstalt, Braunschweig, Germany.

Helv. Phys. Acta 71, Separanda 1 (1998) S7 – S8
0018-0238/98/0100S7-02 $ 1.50+0.20/0

Helvetica Physica Acta

AN ATTEMPT TO PROVE THE DIFFERENCE-QUOTIENT TURBULENCE MODEL

Peter W. Egolf
Swiss Federal Laboratories for Materials Testing and Research, CH-8600 Dübendorf

By introducing the empirically constructed difference-quotient turbulence model (DQM), in the last decade for some problems of simple turbulent flows analytical solutions have been worked out. Now, for an axi-symmetric case a proof of the DQM is outlined, based on physical laws (continuity equation and Navier-Stokes equation) and physical principles (Galilean invariance, self-similarity, isotropy of the turbulence field). A weakness remains, namely the usage of the closure hypotheses.

Up till now the DQM has been presented as an empirically derived model [1], which for different simple flow problems led to several analytical results without empirical constants (see e.g. Ref. [2]). A derivation of the model based on physical principles is demanded.

The continuity equation and the Reynolds equations - derived from the Navier Stokes equations - can be combined to obtain [3]

$$f_{21} = -\beta\frac{1}{\eta}f_1\int_0^{\eta} f_1(\xi)\xi d\xi - \beta\eta(f_{11}-f_{22}) - \beta\eta\int_{\eta}^{\infty}(f_{22}-f_{33})\frac{1}{\xi}d\xi, \qquad \beta = \frac{db}{dx_1}. \tag{1a,b}$$

The quantity b defines the width of the jet, x_1 is the cylindrical co-ordinate on the axis downstream and x_2 on the axis in radial direction (equation 2a). The following self-similarity functions have been assumed to hold

$$\eta = \frac{x_2}{b}, \qquad f_1 = \frac{\overline{u}_1}{\overline{u}_1{}^*}, \qquad f_{ik} = (-1)^{\delta_{ik}+1}\frac{\overline{u_i u_k}}{\overline{u}_1{}^{*2}}, \qquad \delta_{ik} := \begin{cases} 0, & i \neq k \\ 1, & i = k. \end{cases} \tag{2a-d}$$

The function f_1 denotes the dimensionless mean velocity in downstream direction normalized with the center line velocity $\overline{u}_1{}^*$. The f_{ik}'s are dimensionless second-order correlations. With the assumption of isotropy one obtains

$$f_{11} = f_{22} = f_{33}. \tag{3a,b}$$

It can be shown that equation (1a) reduces substantially

$$f_{21} = -\beta\frac{1}{\eta}f_1 g_1, \qquad g_1 = \int_0^{\eta} f_1(\xi)\xi d\xi. \tag{4a,b}$$

Because f_{21} is a second-order correlation and g_1 already occurs in the product with f_1, from the closure assumption it follows that g_1 also must be a function of f_1. In a polynomial approach (the justification is given by equation 9) one obtains

$$g_1 = \sum_{n=0}^{\infty} a_n f_1^{\,n} . \tag{5}$$

With the definitions of the self-similar functions f_i and f_{ik} we obtain

$$\overline{u'_2 u'_1} = b\frac{db}{dx_1}\overline{u}_1 * f_1\left(\sum_{n=0}^{\infty} a_n \overline{u}_1 * f_1^{\,n}\right)\frac{1}{x_2} = b\frac{db}{dx_1}\overline{u}_1\left(\sum_{n=0}^{\infty} a_n \overline{u}_1{}^{*1-n}\,\overline{u}_1^{\,n}\right)\frac{1}{x_2} . \tag{6a,b}$$

In several conventional models gradients of mean velocities occur, which obviously are Galilei invariant. But ordinary velocities do not fulfill this requirement. Therefore, they have to be replaced by velocity differences. Similarly the spatial coordinate x_2 must be replaced by a coordinate difference x_2-x_2*. Then from (6b) it follows that

$$\overline{u'_2 u'_1} = -b\frac{db}{dx_1}(\overline{u}_1 - \overline{u}_{min})\frac{\sum_{n=0}^{\infty} a_n\left(\overline{u}_{1max} - \overline{u}_{1_{min}}\right)^{1-n}\left(\overline{u}_1 - \overline{u}_{1_{min}}\right)^n}{x_{2_{max}} - x_2}, \tag{7}$$

which is a valid alternative solution because

$$x_2{}^* = x_{2_{max}} = 0, \qquad \overline{u}_{1_{min}} = 0, \qquad \overline{u}_1{}^* = \overline{u}_{1_{max}}, \tag{8a-d}$$

where $x_2 = sup\left\{x_2 | \overline{u}_1 = \overline{u}_{1_{max}}\right\}$. An important symmetry requirement is

$$x_1 \to -x_1 \qquad \Leftrightarrow \qquad min \leftrightarrow max, \qquad \overline{u'_2 u'_1}(-x_1, x_2) = -\,\overline{u'_2 u'_1}(x_1, x_2). \tag{9}$$

Equation (7) can only fulfill this symmetry condition if

$$a_1 = -a_0, \ and \qquad a_n = 0, \ \forall n \geq 2. \tag{10a,b}$$

In equation (7) the constant a_0 can be set equal to one, because another constant may always be absorbed by an adjustment of the width b. - Therefore, by applying the general concept of closing a system, in this article it is shown that the DQM is the correct turbulence model to describe the behavior of the axisymmetric turbulent jet.

$$\overline{u'_2 u'_1} = -b\frac{db}{dx_1}(\overline{u}_1 - \overline{u}_{min})\frac{\left(\overline{u}_{1max} - \overline{u}_1\right)}{x_{2_{max}} - x_2} . \tag{11}$$

[1] P. W. Egolf, Phys. Rev. E **49**, 1269 (1994).
[2] P. W. Egolf, D. A. Weiss, Phys. Rev. Lett. **75**, 2956 (1995).
[3] D. B. Taulbee, H. Hussein, article 10-5-1, Sixth Symposium on Turbulent Shear Flows (Toulouse, France, 1987).

Helv. Phys. Acta 71, Separanda 1 (1998) S9 – S10
0018-0238/98/0100S9-02 $ 1.50+0.20/0

Helvetica Physica Acta

UNEXPECTED BOUNDARY CONDITIONS OF LUTTINGER-KOHN ENVELOPE FUNCTIONS FOR A QUANTUM WELL

F. Filipowitz, F.-K. Reinhart

Institute of Micro- and Optoelectronics, Federal Institute of Technology, CH-1015 Lausanne, Switzerland

Luttinger-Kohn envelope functions in the case of a 100 Å quantum well with infinite barriers have been evaluated in the spherical approximation. Though these envelope functions are slowly varying, they are non zero in the barriers. Furthermore they can be discontinuous.

In this paper we claim that the basis introduced by Luttinger and Kohn[1] (LK) to describe holes in perturbed periodic fields is not adapted to solve heterostructure eigenstates.

Review of the theory:

In the case of bulk homogeneous semiconductor, Bloch functions are solutions of the Schrödinger equation $H_c|\psi_{n,\mathbf{k}}\rangle = E_n(\mathbf{k})\cdot|\psi_{n,\mathbf{k}}\rangle$, where H_c is the crystal Hamiltonian containing a spin-orbit coupling term, $E_n(\mathbf{k})$ the energy of the eigenstate $|\psi_{n,\mathbf{k}}\rangle$, The indice n labels the bands and the wavevector $\mathbf{k}$ belongs to the first Brillouin zone of the crystal. The Bloch functions may be written as $\psi_{n,\mathbf{k}}(\mathbf{r}) = e^{i\mathbf{kr}}\cdot u_{n,\mathbf{k}}(\mathbf{r})$, where $u_{n,\mathbf{k}}(\mathbf{r})$ is a function having the lattice periodicity. The position vector is $\mathbf{r}$. Luttinger and Kohn have introduced new functions $\chi_{m,\mathbf{k}}(\mathbf{r}) = e^{i\mathbf{kr}}\cdot u_{m,\mathbf{0}}(\mathbf{r})$ (called the LK functions). They form a complete orthonormal basis if the $\psi_{n,\mathbf{k}}(\mathbf{r})$ do[1].

The Hamiltonian matrix elements of bulk materials are diagonal in the Bloch basis: $\langle\psi_{n,\mathbf{k}}|H_c|\psi_{n',\mathbf{k}'}\rangle = \left[H^B\right]_{n,n'}\cdot\delta_{\mathbf{k},\mathbf{k}'}$, where $\left[H^B\right]_{n,n'} = \left(\frac{(\hbar\mathbf{k})^2}{2\cdot m_{eff,n}(\mathbf{k})} + E_n\right)\cdot\delta_{n,n'}$ and $m_{eff,n}(\mathbf{k})$ is the $\mathbf{k}$-dependent effective mass. E_n is the band edge energy. In the LK basis: $\langle\chi_{m,\mathbf{k}}|H_c|\chi_{m',\mathbf{k}'}\rangle = \left[H^{LK}\right]_{m,m'}\cdot\delta_{\mathbf{k},\mathbf{k}'}$, where $\left[H^{LK}\right]_{m,m'}$ is a non diagonal matrix explicitly given in Ref.1. Each basis has its own advantage: the Hamiltonian matrix element are diagonal in the Bloch basis, whereas the LK parameters describing the effective mass are $\mathbf{k}$-independent in the LK basis. The heterostructure Hamiltonian matrix elements are approximated by position dependent effective mass (or LK parameters) and band edge energies. An effective Bloch or LK Hamiltonian is defined by replacing $\hbar\mathbf{k}$ by the momentum operator and the position vector by the position operator in the heterostructure Hamiltonian matrix elements $\left[H^B\right]_{n,n'}$ or $\left[H^{LK}\right]_{m,m'}$, respectively. Solutions of the Schrödinger equation where Hamiltonian is the effective Bloch (or LK) Hamiltonian are called Bloch (or LK) envelope functions. The transformation of Bloch envelope functions to LK envelope functions is obtained using the matrix elements $\langle\chi_{m,\mathbf{k}}|\psi_{n,\mathbf{k}'}\rangle = s_{m,n}(\mathbf{k})\cdot\delta_{\mathbf{k},\mathbf{k}'}$ that can be explicitly calculated in the spherical approximation using Kane's transformation[2]. The main results of the envelope function approximation[3] is that the projection of the solution $|\psi\rangle$ onto Bloch basis elements, $A_n(\mathbf{k}) = \langle\psi_{n,\mathbf{k}}|\psi\rangle$ are equal to the coefficients to the Fourier coefficients of the Bloch

envelope function: $F_n(\mathbf{r}) = \sum_{n,\mathbf{k}} A_n(\mathbf{k}) \cdot e^{i\mathbf{kr}}$. The same result is valid in the LK basis. In the envelope function formalism, heterostructure eigenstates are established by finding the envelope functions. The solution is then given by $|\psi\rangle = \sum_{n,\mathbf{k}} A_n(\mathbf{k}) \cdot |\psi_{n,\mathbf{k}}\rangle$.

Boundary conditions applied on the envelope functions are therefore of crucial importance to establish correct solutions. As shown by Burt[4], the projection of the solution $|\psi\rangle$ onto Wannier functions is almost equal to Bloch envelope functions. Therefore, Bloch envelope functions are zero in the barriers of a quantum well with infinite barriers.

Results:

We have evaluated Bloch envelope functions of valence electrons close to the Γ_8 symmetry point (heavy and light holes) for a 100 Å quantum well with infinite barriers and interfaces perpendicular to the z-axis, in the spherical approximation and neglecting possible interaction with others bands. Within our notations, the band index n=1,2,3,4 corresponds to an angular momentum of $3\hbar/2$, $\hbar/2$, $-\hbar/2$, $-3\hbar/2$ along the **k**-direction, in the Bloch basis. The band index m=1,2,3,4 corresponds to an angular momentum of $3\hbar/2$, $\hbar/2$, $-\hbar/2$, $-3\hbar/2$ along the z-direction, in the LK basis.

Normalized LK envelope functions corresponding to the n=1 Bloch envelope function have been evaluated using the unitary transformation $s_{m,n}(\mathbf{k})$. Results are shown on Fig.1 ($\mathbf{k}_x=\mathbf{k}_y=0$) and Fig.2 ($\mathbf{k}_x\neq0$, $\mathbf{k}_y=0$).

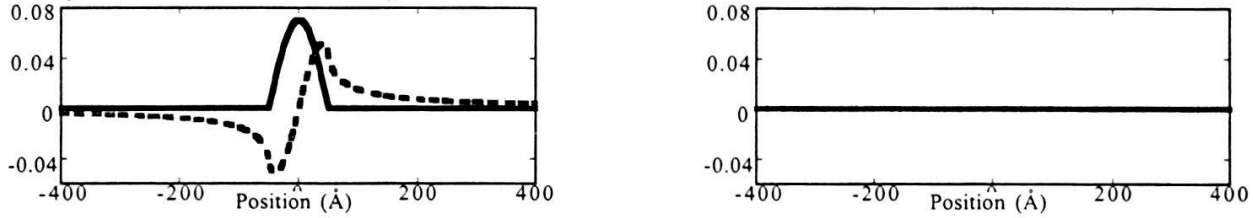

FIG.1. Real (–) and imaginary (--) part of the normalized LK envelope functions corresponding to the projection of the n=1 Bloch envelope function onto the m=1 band (left graph) and m=2 (right graph). ($\mathbf{k}_x=\mathbf{k}_y=0$)

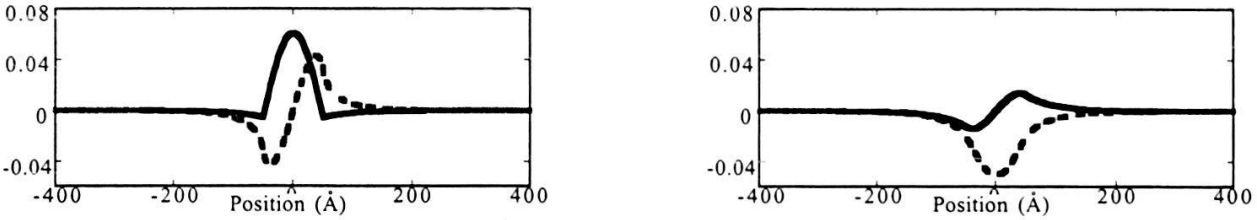

FIG.2. Real (–) and imaginary (--) part of the normalized LK envelope functions corresponding to the projection of the n=1 Bloch envelope function onto the m=1 band (left graph) and m=2 (right graph). ($\mathbf{k}_x=0.02$ (1/Å), $\mathbf{k}_y=0$)

The LK envelope functions are non-zero in the barriers and can be discontinuous at the interface (Fig.2, left graph). These points, mentioned in Ref.5, show that the LK basis is not adapted to find heterostructure envelope functions.

References:

[1]J.M. Luttinger and W. Kohn, Phys. Rev., **97**, 869 (1955).

[2]E.O. Kane, J. Phys. Chem. Solids, **1**, 249 (1957).

[3]M. Altarelli, in *Heterojunctions and Semiconductors Superlattices*, (a. G.Allan Eds.), Springer-Verlag, Berlin and New York, pp. 12-37, (1985).

[4]M.G. Burt, J. Phys:Condens. Matter, **4**, 6651 (1992).

[5]M.J. Godfrey and A.M. Malik, Phys. Rev. B, **53**, 16504 (1996).

Helv. Phys. Acta 71, Separanda 1 (1998) S11 – S12
0018-0238/98/0100S11-02 $ 1.50+0.20/0

Helvetica Physica Acta

RESULTS OF GEODETIC TIME TRANSFER ON AN EUROPEAN BASELINE

F. Overney, L. Prost, Th. Schildknecht†, G. Beutler†, J. A. Davis††, J. M. Furlong††

Swiss Federal Office of Metrology, Lindenweg 50, 3084 Wabern, Switzerland
† Astronomical Institute of the University of Berne, Sidlerstrasse 5, 3012 Berne, Switzerland
†† National Physical Laboratory, Queens Road, GB-TW11 OLW Teddington, United Kingdom

Accuracy in time metrology not only depends on the performances of the atomic clocks but also on the time and frequency comparison capabilities. First results of the comparison of different atomic clocks carried out between European laboratories using a new method, called Geodetic Time Transfer, are reported.

Up to now, the two most used methods in the time transfer domain are the so-called common-view (CV) [1] and the Two-Way Satellite Time and Frequency Transfer TWSTFT [2]. The first one is rather simple to use but limited to a precision of few nanoseconds for observation time of 1 day and does not permit the precision required to compare the clocks at their best performance. The second is more precise (typically 50 ps at τ=300 s) but relatively complicated and expensive to use. Furthermore, the cost of the satellite time often makes continuous TWSTFT comparisons between clocks prohibitively expensive.

Like the CV method, the Geodetic Time Transfer method (GeTT) [3] uses the satellites of the Global Position System (GPS) and hence is also relatively simple and cheap to use. In contrast to the CV, the GeTT takes full advantage of the potential of the GPS signals: all five observables are taken into account, all satellites in view are tracked and the data are processed in an interferometric mode. Adapted from geodetic techniques, this method permits a theoretical precision of some 10 ps and the accuracy should reach the subnanosecond level.

GeTT measurements were carried out between the Swiss Federal Office of Metrology (OFMET) and the National Physical Laboratory (NPL) during 47 days (MJD: 50686-50733) without interruption. The baseline between both laboratories has a length of about 750 km. The GeTT terminal at the OFMET was driven by the cesium clock Cs#1. At NPL, the GeTT terminal was steered by one of two H-masers SIGMA TAU of the laboratory.

Figure 1 shows the square root of the Allan variance (σ_y) of the measurements. An estimate of the Allan variance of the Cs#1 has been computed using a linear combination of the comparison of the Cs#1 against a set of six cesium clocks also located at OFMET. For the GeTT measurement, the Allan variance was directly computed from the GeTT results obtained from the phase L3 observation over a 19 day-period (MJD: 50696-50715). σ_y[Cs#1-Hmaser] computed from the GeTT(L3) measurements is in excellent agreement (for τ<2-3 days) with the estimate for Cs#1 alone. First, this means that the noise is entirely dominated by the noise of Cs#1 as expected for a short integration time. Second, these results show that, over a baseline of 750 km, GeTT has a lower instrumental noise than commercial, high-performance cesium clocks. This implies, that GeTT is well suited for comparison of these kind of clocks.

For τ>3 days, one observes an apparent discrepancy between the two Allan variances shown in Figure 1: the comparison appears to be better than the performance of Cs#1 alone ! Three reasons might explain this difference:

a) The data used in the calculation were not taken over the same period for both curves. Therefore, a change in the behaviour of the clock could induce such a difference.
b) The method used to estimate σ_y[Cs#1] (linear combination of different clock comparisons) could introduce some error.
c) Another unknown parameter is the long-term noise of the phase comparator used in the local comparison of cesium clocks, namely the effect of the variation of the room temperature.

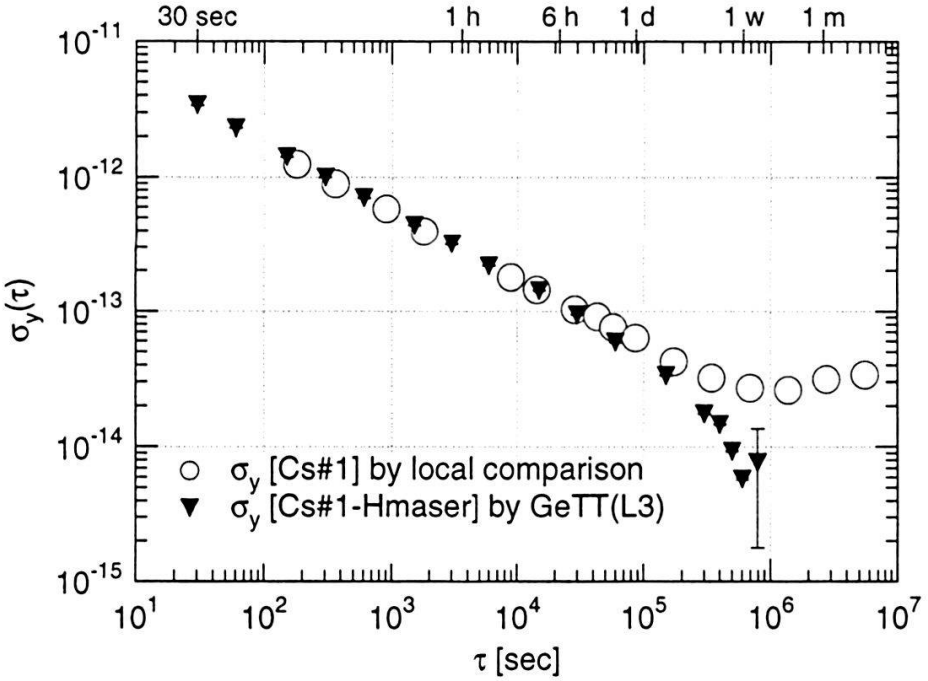

Fig. 1: Square root of the Allan variance computed for the Cs#1-Hmaser comparison (filled triangle) and for Cs#1 alone (open circles).

The experiment has shown that the instrumental noise of the GeTT technique over a 750 km baseline and time intervals of 10 days is lower than the noise of commercial, high performance cesium clocks. We actually expect the instrumental noise to be lower by a factor of 10. The method is also very promising for the comparison of high performance frequency standards especially due to its unique resolution for time intervals between 30 to 10^5 seconds.

[1] N.Ashby, M. Weiss, "Accurate time transfer during common-view of a GPS satellite", Proc. 34th Ann. Symp. on Frequency Control, pp. 334-346, 1980.
[2] D. Kirchner, "Two-Way Time Transfer Via Communication Satellites", in Proc. IEEE, Vol. 79, No 7, pp. 983-989, 1991
[3] Th. Schildknecht et al., G. Beutler, W. Gurtner, M. Rothacher, "Towards sub-nanosecond GPS Time Transfer using Geodetic Processing Technique", Proc. 4th EFTF, pp. 335-346, 1990.
[4] F. Overney, Th. Schildknecht, G. Beutler, L. Prost, U. Feller, "GPS Time Transfer Using Geodetic Receivers: Middle-Term Stability and Temperature Dependence of the Signal Delays", Proc. 11th EFTF, pp. 504-508, 1997.

Helv. Phys. Acta 71, Separanda 1 (1998) S13 – S14
0018-0238/98/0100S13-02 $ 1.50+0.20/0

Helvetica Physica Acta

Experimental electronic structure of a 1D organic metal: TTF-TCNQ

F. Zwick[1], M. Grioni[1], M. Onellion[2], G. Margaritondo[1]
[1]*Institut de Physique Appliquée, EPFL, CH-1015 Lausanne*
[2]*Department of Physics, University of Wisconsin, Madison WI 53706, USA*

We exploited angle-resolved photoelectron spectroscopy (ARPES) with high energy resolution to map the band structure of the typical one-dimensional organic conductor TTF-TCNQ. We directly observe dispersing spectral features corresponding to the donor (TTF) and acceptor (TCNQ) bands, and their crossing at the Fermi wavevector k_F. Near the chemical potential, however, the quasiparticle peak are completely renormalized away, and the spectrum is totally incoherent. The suggest that we have observed the dispersion and spectral function of a metallic non-Fermi liquid.

Quasi one-dimensional (1D) conductors have recently attracted much interest, following theoretical suggestions that the usual Fermi liquid description of the electronic properties may break down, and be replaced by the Luttinger liquid scenario. Angular resolved photoemission spectroscopy (ARPES) is a promising technique to investigate this issue. We present here a brief summary of an ARPES investigation of a typical 1D organic conductor: TTF-TCNQ. In this material, segregated 1D chains are formed along the crystallographic **b** direction by the stacking of the planar TTF and TCNQ molecules. Molecular orbitals overlap and form 1D bands along this direction. Charge (0.55 electrons per molecule) is transferred from the TTF (donor) to the TCNQ (acceptor) chain, yielding two partly filled bands crossing each other at the Fermi level. Thus, the electronic properties are strongly anisotropic and very metallic along b in the normal state. The system then undergoes at T_P=54 K a Peierls transition. A charge density wave (CDW) accompanied by a periodic lattice distortion (PLD) is developed. Further CDW transitions lead the system into a insulating groundstate [1].

The experiments were performed at the Wisconsin Synchrotron Radiation Center in Wisconsin and with a Scienta ESCA-300 spectrometer in Lausanne. We measured high quality single crystals mounted on a cold stage and cleaved in UHV. The temperature was varied between 30 K and RT. We used linearly polarized synchrotron radiation ($h\nu$=20 eV) and 21.2 eV photons from a He discharge lamp. The energy resolution was 15 meV (including thermal broadening) and the angular resolution was ±1°.

Fig. 1 shows the ARPES data for TTF-TCNQ, along the chain direction. We observe a spectral feature dispersing towards E_F away from Γ (the zone center), and then back to 0.75 eV at Y (the zone boundary). The same state does not disperse at all along a the direction perpendicular to the chains (data not shown). We interpret this dispersive feature as an image of the TCNQ and TTF bands, forming pockets around Γ and Y. The crossing of the two bands at $k_F=\pm(0.25\pm0.02)$Å^{-1}, is in excellent agreement with band calculations, and experimental determinations of the CDW wavevector [2]. However, strictly speaking, no Fermi surface can be determined

since the feature never comes closer than 0.2 eV to E_F. Instead the spectral weight near E_F is completely suppressed at E_F. These observations contrast with the usual Fermi liquid picture, where a quasi particle state disperses through the Fermi level. Also, the spectral lineshape is incompatible with standard quasiparticle lineshapes.

Fig. 2 shows data taken at $k=k_F$ at 70 K and at 30 K, in the CDW phase. The leading edge of the peak shifts back by Δ=20meV at 30K, revealing the opening of a real Peierls gap. At 70 K a pseudogap is well developed above. Precursor fluctuations of the CDW state could explain the pseudogap between T_P and the meanfield temperature $T_{MF} \approx 160$ K. However, in our case even above T_{MF} the pseudogap is visible (not shown).

These spectral properties indicate that TTF-TCNQ is certainly not a "normal" metal. Work is in progress to understand the origin of this unusual behavior, namely to relate it to independent evidence for strong electronic correlations in this material.

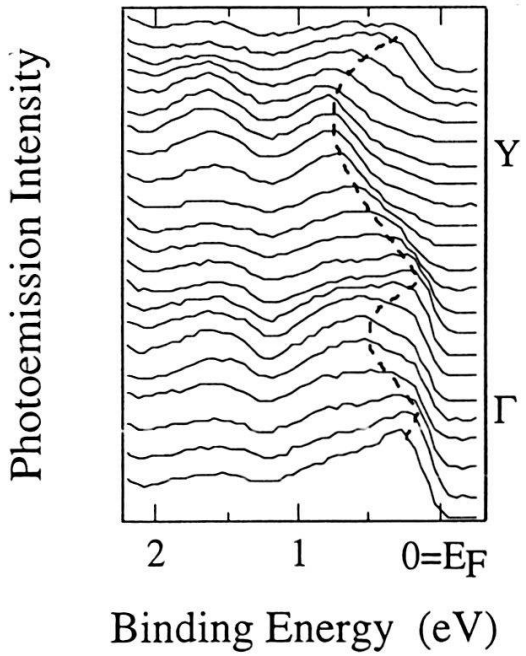

Fig. 1. ARPES spectra of TTF-TCNQ, along the 1D chain direction. The temperature was 150 K. The photon energy was 20 eV.

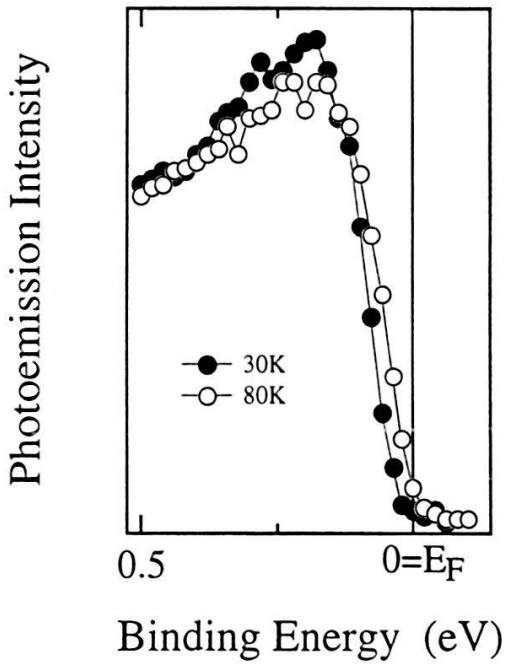

Fig. 2. ARPES spectra at $k=k_F$ as a function of temperature. The energy shift reveals a real Peierls gap of ~20 meV. The photon energy was 21.2 eV.

References:

[1] D. Jérome and H. J. Schulz, Adv. Phys. **31**, 299 (1982).
[2] J. P. Pouget et al., Phys. Rev. Lett. **37**, 437 (1976).

Helv. Phys. Acta 71, Separanda 1 (1998) S15 – S16
0018-0238/98/0100S15-02 $ 1.50+0.20/0

Helvetica Physica Acta

Divergence of the dielectric function with the delocalization transition of quantized 2D electrons

M. Furlan

Swiss Federal Office of Metrology, CH-3084 Wabern, Switzerland; and
EPFL, Institut de micro- et optoélectronique, CH-1015 Lausanne, Switzerland

The fundamental length scale ξ of electron localization in high mobility GaAs/AlGaAs heterostructures was determined from transport measurements in the quantum Hall regime. For the first time, we clearly observed the divergence of ξ over a wide range of filling factors, with the Fermi energy approaching a Landau level centre. Two models, based on variable-range hopping theory, are compared. A divergence of the dielectric function $\varepsilon_r \propto \xi$ is derived.

Electron transport of a quantized 2D electron gas at very low temperatures can be described by a theory of variable-range hopping (VRH) [1]. In this regime, conductance via electrons, which are thermally activated to the next extended states, is exponentially small. Taking into account a Coulomb gap in the density of states, the longitudinal hopping conductivity in two dimensions is expected to follow

$$\sigma_{xx}(T) = \sigma_0 \, e^{-(T_0/T)^{1/2}} \quad \text{, where} \quad k_B T_0 = C \, \frac{e^2}{4\pi \, \varepsilon_r \, \varepsilon_0 \, \xi} \, , \tag{1}$$

with the numerical constant $C \approx 6.2$, the dielectric function $\varepsilon_r \approx 13$ (value for GaAs), the vacuum permittivity ε_0 and the localization length ξ. The simplifying assumption of a constant ε_r is, however, not necessarily correct, as discussed below.
An increasing Hall electric field $\vec{E}_H$ (as a consequence of increasing bias current J) forms a local Fermi distribution equivalent to an effectively enhanced electron temperature $T_{eff} \propto \vec{E}_H \, \xi$, leading to non-Ohmic characteristics [2]. The electric field dependent longitudinal conductivity is then expressed by

$$\sigma_{xx}(\vec{E}_H) = \sigma_1 \, e^{-(\vec{E}_0/\vec{E}_H)^{1/2}} \quad \text{with} \quad \vec{E}_0 = 2 \, \frac{k_B T_0}{e \, \xi} \, . \tag{2}$$

The characteristic field value $\vec{E}_0$ is seen to be directly related to the hopping temperature T_0 and inversely proportional to ξ. Thus, both the temperature and current dependent VRH conductivities explicitly depend on the localization length, allowing to determine ξ from two different experiments.

We have performed extensive transport measurements on high mobility GaAs/AlGaAs heterostructures in the temperature range $T = 0.3 \ldots 20$ K and at magnetic fields of 3...10 T. Electron conduction was found to be dominated by VRH at $T \leq 1.4$ K. The localization length ξ as a function of the filling factor $\nu = 2\pi \, \ell_B^{\,2} \, n_e$ (where ℓ_B is the magnetic length and n_e the electron sheet density) was derived either directly from the temperature dependent $\sigma_{xx}(T)$ with Eq.(1) or by comparison of the temperature and current dependent conductivities, relating an effective electron temperature to the applied current density (cf. Eq.(2)). Typical results obtained for one sample are shown in Fig.1 for $\nu = 1.5 \ldots 4.5$ (missing data points in the centres of the quantized plateaus are due to unmeasurably small σ_{xx} values). A divergence of ξ with the Fermi energy approaching the

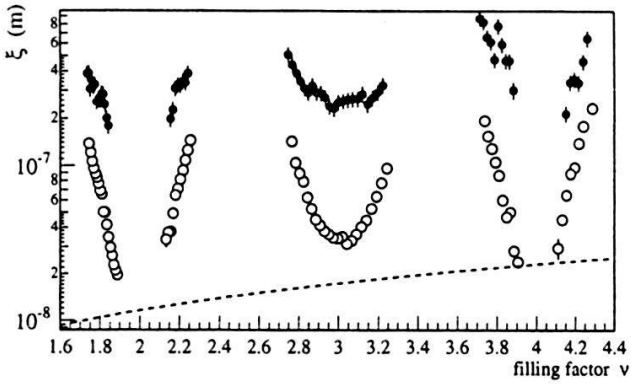

Figure 1: Localization length ξ as a function of the filling factor ν, determined from the temperature (open circles) or current (full dots) dependent σ_{xx}. The dashed line corresponds to the classical cyclotron radius.

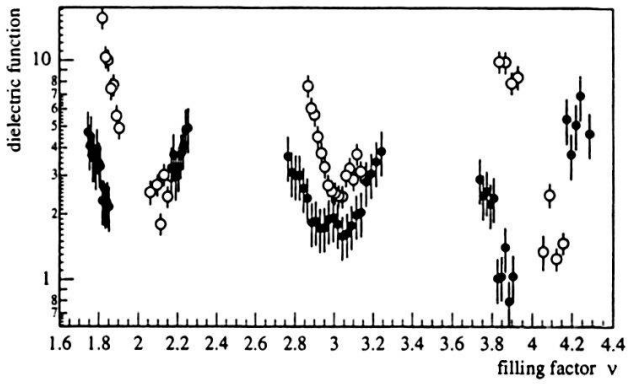

Figure 2: The ratio $\xi(T)/\xi(J) \propto \varepsilon_r$, yielding the dielectric function (dots and circles representing two different samples).

Landau level centres (approximately at half filling fractions) is clearly observed. In the quantized regime around the conductivity minima, the values $\xi(T)$ are well on the order of the length of the classical cyclotron radius (dashed line in Fig.1), as predicted recently by theory [3]. In contrast, $\xi(J)$ was found to be too large by typically one order of magnitude. This is attributed to an underestimate of $\vec{E_0}$ due to an inhomogeneous electric field distribution, which can be understood either within percolation network theories or as a consequence of edge current effects. For the latter case, we extrapolate a width of dominant potential drop at the sample edge of about 100 μm.

The spin gap (around odd ν between spin-split Landau levels) is sufficiently small to allow the observation of the power law divergence $\xi(\nu) \propto |\nu\text{-}\nu_c|^{-\gamma}$ as predicted from scaling theories of electron localization, with a critical exponent $\gamma \approx 2.3$ [4]. From our experiments, we derive a value of $\gamma(T) = 4.61 \pm 0.24$ and $\gamma(J) = 2.29 \pm 0.21$ for the temperature and current dependent data, respectively. Furthermore, the ratio $\xi(T)/\xi(J)$, which is shown in Fig.2, was found to be proportional to $\xi(J)$. The extracted dielectric function ε_r (appearing in Eq. (1)) agrees with the commonly used static value at the plateau centres ($\xi(T)/\xi(J)$ close to unity), but increases with decreasing distance to the next Landau level centre. From these results, we conclude that the dielectric function in a quantized 2D electron gas diverges with ν like $\varepsilon_r \propto \xi^{\beta}$, with $\beta = 1.098 \pm 0.096$. Whereas such behaviour has been reported for the 3D case [5], this is the first experimental evidence for a diverging ε_r in two dimensions observed in a quantum Hall system.

[1] B. I. Shklovskii and A. L. Efros, *Electronic Properties of Doped Semiconductors* (Springer, Berlin, 1984).
[2] B. I. Shklovskii, Fiz. Tekh. Poluprovodn. **6**, 2335 (1972) [Sov. Phys. Semicond. **6**, 1964 (1973)].
[3] M. M. Fogler, A. Yu. Dobin, and B. I. Shklovskii, preprint cond-mat/9707232.
[4] H. P. Wei, D. C. Tsui, M. A. Paalanen, and A. M. M. Pruisken, Phys. Rev. Lett. **61**, 1294 (1988); G. V. Mil'nikov and I. M. Sokolov, Pis'ma Zh. Eksp. Teor. Fiz. **48**, 494 (1988) [JETP Lett. **48**, 536 (1988)]; J. T. Chalker and P. D. Coddington, J. Phys. C **21**, 2665 (1988).
[5] see, for instance: Y. Imry, in *Anderson Localization*, edited by Y. Nagaoka and H. Fukuyama (Springer, Berlin, 1984) p.138, and references therein.

Helv. Phys. Acta 71, Separanda 1 (1998) S17 – S18
0018-0238/98/0100S17-02 $ 1.50+0.20/0

Helvetica Physica Acta

Metal to insulator transition of K-Sn Zintl system investigated by ultraviolet photoelectron spectroscopy

By
A. Gremaud, J. Geng, A. Schüler, G. Indlekofer, P. Oelhafen

Institut für Physik, Klingelbergstrasse 82
CH-4056 Basel

Abstract. Due to structural effects the intermetallic phases of certain alloys of alkali and polyvalent metals reveal a metal to non-metal transition as a function of concentration ratio. This transition is observed by valence band spectroscopy on $K_x\ Sn_{1-x}$ thin films with synchrotron radiation.

The properties of alloys of alkali metals with metallic polyvalent metals (i.e. elements of group III b and IV b) were first investigated by E. Zintl in the late 1930s [1]. In the crystalline phase the structure is dominated by a tetrahedral arrangement of the atoms of the polyvalent metal with alkali atoms placed opposite to the faces of the tetrahedron. The chemical bond of the alkali to the polyvalent metal is in this case more similar to the ionic than to the metallic type, the resistivity of the alloy being considerably increased. Charge is transferred from the alkali atoms to the polyvalent metal tetrahedron, which is therefore often referred to as a Zintl-anion $(A)_4^{4-}$, where A is a polyvalent metal. More recent experiments [2] on the liquid phase revealed a significant increase of the electrical resistivity at the same stoichiometries (i.e. 50 % in most cases) as in the crystalline phase. This suggests the existence of an intermediate disordered structure in which dependent on the concentration ratio at least a part of the polyvalent atoms are bound in Zintl anions or fragments thereof. This view is supported by ab initio calculations on similar systems, e.g. [3].

The photoemission experiments presented here were carried out at the high-resolution low energy beamline SU3 at Super-ACO, Orsay. Films of K-Sn alloys were prepared by co-evaporation at 77 K on quarz substrates at base pressures better than $2 \cdot 10^{-10}$ mbar. High purity Sn was evaporated from an Omicron EFM3 source and K was dispensed using alkali metal dispensers from SAES, their mounting was cooled with liquid nitrogen. The oxygen content – less than ≈ 2 % – was determined by XPS Mg Kα spectra taken after the valence band and shallow core levels and therefore can be considered as an upper limit.

The figures below show a sequence of films with increasing K contents. Sn 4d and the K 3p measured at $h\nu = 70eV$ were used for the determination of the relative atomic con-

centrations with the photoionization cross-sections of [4]. Besides rescaling for presentation purposes and energy shift correction, no data processing has been applied to the spectra. Figure 1 shows the valence band spectra of K-Sn for concentration ratios over the complete range. The valence band edge is shown in detail in figure 2. The pseudo-gap at K concentrations around 50% indicates a metal-insulator-metal transition which is in good qualitative agreement with the resistivity measurements of the liquid phase by Xu et al [2]. The transition occurs at the same concentration ratio as in the liquid, and the concentration range over which the system is non-metallic is very similar. This overall similarity with the liquid system strongly suggests a disordered structure of the solid alloy similar to the structure in the liquid.

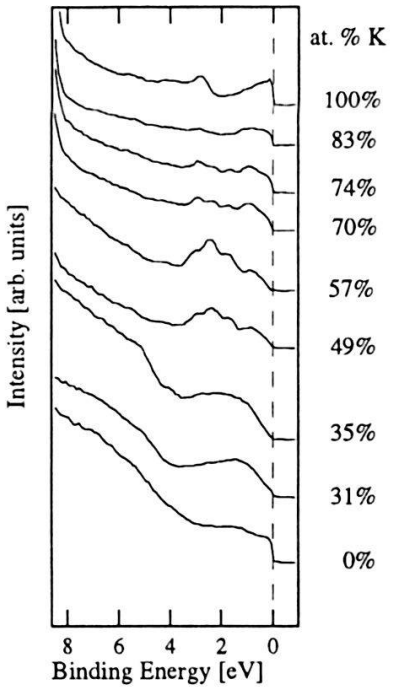

Figure 1: Valence band spectra of $K_x\ Sn_{1-x}$ ($h\nu$ = 27eV). The intense rise in intensity near 8 eV is due to the K_{MVV} Auger transition.

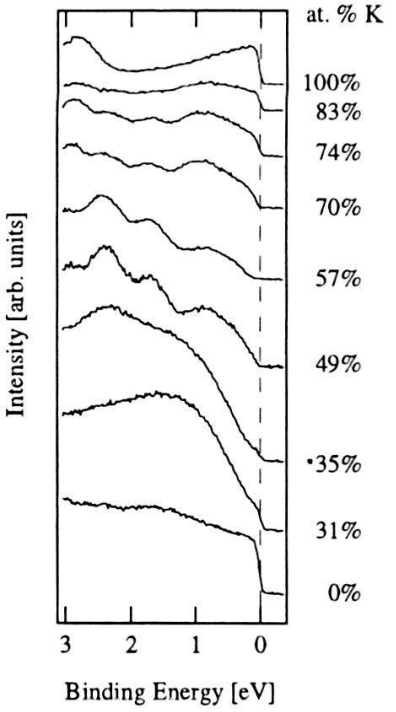

Figure 2: The valence band edge with smaller energy steps (10 mV). (same photon energy $h\nu$ = 27eV and analyzer settings as in Figure 1, CAE = 5 eV, $\Delta E \approx$ 20 meV)

References

[1] E. Zintl. Intermetallische Verbindungen. *Angewandte Chemie*, 52(1):1 - 48, 1939.

[2] R. Xu, T. de Jonge, and W. van der Lugt. The electrical resistivities of liquid K–Sn and Cs–Sn alloys. *J. Non-Cryst. Solids*, 156 - 158:293 - 296, 1993.

[3] Giulia Galli and Michele Parrinello. Theoretical study of molten KSi. *J. Chem. Phys*, 95(10), 1991.

[4] J. J. Yeh and I. Lindau. Atomic subshell photoionization cross sections and asymmetry parameters. *Atomic data and nuclear data tables*, 32(1):1 - 155, 1985.

Helv. Phys. Acta 71, Separanda 1 (1998) S19 – S20
0018-0238/98/0100S19-02 $ 1.50+0.20/0

Helvetica Physica Acta

A Combined Confocal and Scanning Near-Field Optical Microscope as an Analysis Tool in Life Sciences

J.M. Freyland, R. Eckert, Th. Huser, R. Rodrigues-Herzog and H. Heinzelmann
Physics Department, University of Basel, 4056 Basel, Switzerland

We have designed a versatile optical microscope that allows quick identification of small interesting areas on large samples using confocal microscopy and subsequent high-resolution imaging by scanning near-field optical microscopy. First results on fluorescence-labeled μ-contact printed rabbit IgG are shown.

For the last 100 years light microscopy has been an indispensable tool in life sciences. Its continuously increased resolution has reached Abbé's fundamental diffraction limit of $\lambda/2$ providing biologists with insight in the microscopic structure and dynamics of life on the sub-micrometer scale. The trend in modern molecular biology towards even smaller sample features requires a resolution better than 100 nm. One of the most promising methods to achieve this is Scanning Near-Field Optical Microscopy (SNOM) [1, 2] where the sample is illuminated through a fiber tip with an aperture smaller than 100 nm. This tip is raster-scanned over the surface in distances of a few nm. The optical resolution then depends primarily on the size of the aperture. Recently we manufactured SNOM probes with unprecedented control over uniformity and aperture size by focused ion beam (FIB) milling (fig. 1). In this article we describe a combined laser scanning confocal microscope (CLSM)

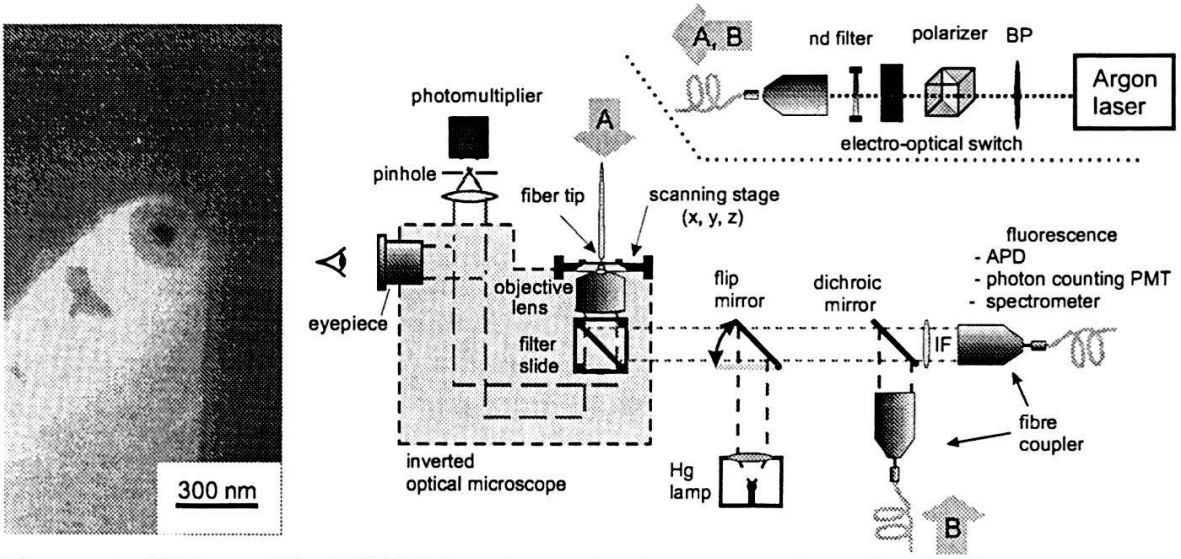

Figure 1: FIB modified SNOM probe and schematics of the SNOM/CLSM setup.

and SNOM suitable for fluorescence imaging of biological samples. Confocal microscopy is a well-established far-field method which allows imaging of large areas in reasonable time (CLSM-mode). This is especially useful for locating interesting features on large samples. Subsequently these features can be investigated by high resolution near-field microscopy (SNOM-mode), providing additional information on the topography of the sample.

The basis of our setup consists of an inverted optical microscope (fig.1). The sample is mounted on a closed-loop (x,y,z)-scanning stage above a microscope objective. Under

the objective a standard filter slide with three filter/mirror sets is placed allowing for quick switching between the three operation modes: CLSM-, SNOM-mode or conventional fluorescence microscopy (Hg-lamp). In CLSM- and SNOM-mode the sample is illuminated by a tunable Ar^+-laser, which can be blocked by an electro-optical switch when no illumination is wanted, e.g. during the back scan, minimizing fluorescence bleaching dramatically. A single-mode fiber connects the laser either to **A** (SNOM-mode) or **B** (CLSM-mode)(fig. 1).

In CLSM-mode the excitation light (**B**) is reflected by a dichroic mirror into the inverted microscope and focused onto the sample. Fluorescence and backscattered excitation light are collected by the same objective. The dichroic mirror and an interference filter (IF) separate the fluorescence from the excitation light. The fluorescence light is then coupled into a multi-mode fiber and analyzed by an APD or a spectrometer. In this setup the pinhole for confocal detection is substituted by the fiber end.

In SNOM-mode the excitation light (**A**) is led through a SNOM fiber onto the probe. The fluorescence and transmitted excitation light are collected by the objective lens. A dichroic mirror and a short-pass filter in the filter slide separate them. In order to reduce detection of straylight the excitation light is focused through a pinhole onto a photo-multiplier. The detection of the fluorescence light is done in analogy to the CLSM-mode. For distance control of the fiber tip a non-optical shear force scheme that utilizes a tuning fork and phase sensitive feedback is used [3]. Tip and tuning fork are mounted on a tripod that permits easy approach.

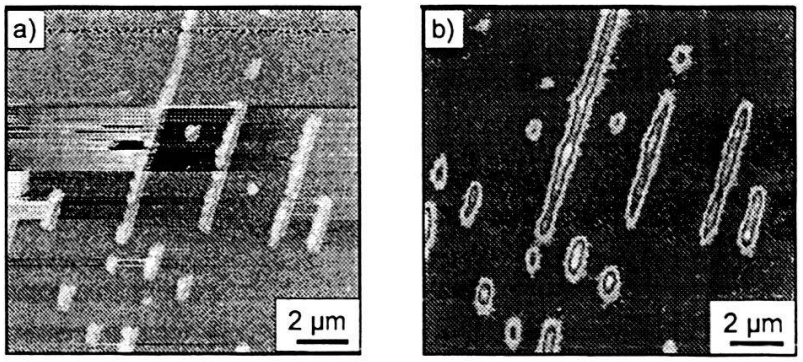

Figure 2: (a) topography and (b) fluorescence image of contact printed rabbit IgG.

Fig. 2 shows SNOM images of a mono-layer of fluorescein labeled rabbit IgG on glass. The structure was produced by a μ-contact printing method [4]. The maximum fluorescence signal was about 200 counts/10ms integration time, demonstrating that our instrument is capable of imaging weak signals from delicate biological samples. Future applications include single molecules experiments and imaging of YOYO-1 labeled DNA.

We acknowledge J.Brugger and P.Vettiger for preparing the FIB modified SNOM probes and D.Anselmetti for providing the samples.

References

[1] Pohl, D.W. et al., Appl. Phys. Lett. **44**, 651 (1984).

[2] Heinzelmann, H. and Pohl, D.W., Appl. Phys. A **A59**, 89 (1994).

[3] Ruiter, T.M. et al., Appl. Phys. Lett. **71**, 28 (1997).

[4] Bernard, A. et al., submitted to Langmuir

Helv. Phys. Acta 71, Separanda 1 (1998) S21 – S22
0018-0238/98/0100S21-02 $ 1.50+0.20/0

Helvetica Physica Acta

Three-Dimensional Densitometric Quantification of Arterial Stenoses

P.-A. Doriot, P.-A. Dorsaz, L. Dorsaz

University Hospital, Cardiology, Geneva, Switzerland

The quantification of coronary artery stenoses in angiographic images plays a dominant role in interventional cardiology. Unfortunately, the geometric methods used to this purpose are not accurate. To overcome their limitations, several densitometric techniques have been developed. They assume, however, that the X-rays are perpendicular to the vessel axis in space, and that the relationship between local thickness of contrast medium in the vessel and resulting "densitometric signal" is linear. Since these two conditions are seldom fulfilled, we have developed an improved densitometric method featuring a combined correction for these two types of error contributions.

In interventional cardiology, the reduction percentage of the normal arterial diameter at a stenosis plays an essential role in evaluating the necessity and success of an angioplasty procedure. Alternatively, one can also use the reduction percentage of the lumen area. These parameters can be determined in the digital angiographic images with the help of computer assisted methods. In the "geometric" methods, the most frequently applied ones, the vessel lumen is assumed circular, which is often unrealistic, especially for balloon dilated lumens. To overcome this basic limitation of geometric approaches, densitometric techniques have been developed. While they are not sensitive to the actual shape of the lumen, they require, however, orthogonality between vessel axis and X-rays, as well as a linear relationship between local contrast medium thickness in the vessel and resulting "densitometric signal" [1] (The densitometric signal S(t(P)) in a pixel P on the vessel shadow is defined by $S(t(P)) = C [\ln I_{bg}(P) - \ln I(t(P))]$ where t(P) is the contrast medium thickness in the vessel along the X-ray beam associated to pixel P ; C is a calibration constant which depends on the (arbitrary) gray level units ; $I_{bg}(P)$ is the gray level (often called "Intensity") of the background in pixel P, and I(t(P)) is the gray value of P.

To fulfill the requirements of orthogonality and linearity in the cardiac catheterization laboratory is practically impossible. We have therefore developed a combined correction applicable at subsequent image analysis which takes the actual orientation of the X-rays relatively to the vessel axis into account as well as non linear effects. Because it implies 3-D reconstruction of the vessel segment of interest, it requires the acquisition of nearly simultaneous images in two projections (called planes 1 and 2 in the following), and the filming of an appropriate calibration object bearing markers at known locations. We use thereto a cube with small steel balls at the corners and at center points [2].

To determine the angles β_1 and β_2 between the vessel axis in space and the X-rays of planes 1 and 2, the vessel centerline is 3-D reconstructed by using the corresponding centerlines determined in images 1 and 2. Similarly, determination of the vessel edges in the two images leads to two diameter values, d_1 and d_2 (in mm), at each spatial centerline point [2].

In designing the part correcting for non linearity, the first step was to investigate the relationship between contrast medium thickness t and resulting densitometric signal S(t). This was done for the 2 x 2 imaging chains of our 2 biplane angiocardiographic equipment (2 x Bicor/Hicor, Siemens). It turned out that this relation can be sufficiently well approximated (for a given contrast agent) by a single 9^{th} order polynomial, independently of particular conditions such as patient transparency, actual projection, kV, magnification mode, etc. Under the assumption that the

vessel cross section is circular, knowledge of the apparent vessel "diameter" d_1 (respectively d_2) and of the angle β_2 (resp. β_1) between the vessel axis and the X-rays of plane 2 (resp. 1) allows to calculate a correction factor $f_{cor}(d_1,\beta_2)$ (resp. $f_{cor}(d_2,\beta_1)$) which corrects the erroneous "densitometric area" $A_{1,dens}$ (resp. $A_{2,dens}$) into a more accurate value A_1 (resp. A_2) according to the formula :

$f_{cor}(d_1,\beta_2) = \text{Sum} [f_i (d_1)^{i-1} / \sin^i \beta_2]$, i = 0 to 9 , respectively :

$f_{cor}(d_2,\beta_1) = \text{Sum} [f_i (d_2)^{i-1} / \sin^i \beta_1]$, i = 0 to 9 (The values of the f_i are given in [3])

This combined correction was evaluated by means of a phantom consisting of two discs in which 2 x 5 radial channels with diameters ranging from 0.80 mm to 4.00 mm were filled with contrast medium. Combination of the 5 largest cross sectional areas with all smaller ones to pairs according to the formula

$D_{true}(k,j) = 100 \times [A_{true}(k) - A_{true}(j)] / A_{true}(k)$, (k = 6 to 10 ; j = 1 to 9 ; $A_{true}(k) > A_{true}(j)$)

yielded 35 area reduction percentages $D_{true}(k,j)$ ranging from 11 % to 96 %.

The two discs were placed in water baths of 10 to 29 cm thickness and filmed with various orientations against each other, and under various pairs of incidences. For each projection pair, the cube was filmed with exactly the same biplane geometry. The native densitometric areas and the diameters of the 10 channels were then determined in all recorded projections, and the experimental area reduction percentages corresponding to the 35 $D_{true}(k,j)$ were calculated.

The correlations between the 35 $D_{true}(k,j)$ and the 525 corresponding experimental values obtained without and with correction of the native densitometric areas were:

Without correction	Plane 1 :	$D(k,j) = 1.04\ D_{true}(k,j) - 4$ % ,	r = 0.97 ,	SEE = 6 %
	Plane 2 :	$D(k,j) = 1.06\ D_{true}(k,j) - 6$ % ,	r = 0.98 ,	SEE = 6 %
With correction	Plane 1 :	$D(k,j) = 1.02\ D_{true}(k,j) - 0$ % ,	r = 0.99 ,	SEE = 3 %
	Plane 2 :	$D(k,j) = 1.02\ D_{true}(k,j) - 0$ % ,	r = 0.99 ,	SEE = 4 %

To assess the effect of the correction on data of patients, two sets of 10 stenoses each were picked out of a collective of coronary stenoses which had previously been analyzed in the context of another study. The first set consisted of the 10 stenoses which exhibited initially the largest interplane discrepancies. The second set consisted, on the contrary, of the 10 stenoses which exhibited the lowest interplane discrepancies. Correcting the first set only for inadequate X-ray orientation reduced the initial discrepancies. Alternatively, applying the combined correction produced a slightly greater improvement. This indicates that non linear effects are (fortunately) not an important source of inaccuracy in patients. Correcting the second set only for inadequate X-ray orientation augmented slightly the initial discrepancies. Application of the combined correction let them unchanged ; this means that the combined correction does not degrade the accuracy.

References

[1] P.-A. Doriot, N. Guggenheim, P.-A. Dorsaz, W. Rutishauser: Morphometric versus densitometric assessment of coronary vasomotor tone - An overview. Eur. Heart J. 10 (Suppl. F): 49-53, 1989.

[2] N. Guggenheim, F. Chappuis, C. Suilen, P.-A. Doriot, P.-A. Dorsaz, P. Descouts, W. Rutishauser: 3D-reconstruction of coronary arteries in view of flow measurement. Int J Cardiac Imaging 8: 265-272, 1992.

[3] P.-A. Doriot, P.-A. Dorsaz, L. Dorsaz: Toward a gold standard for quantitative coronary arteriometry. Phys. Med. Biol. 42: 2449-2462, 1997.

Helv. Phys. Acta 71, Separanda 1 (1998) S23 – S24
0018-0238/98/0100S23-02 $ 1.50+0.20/0

Helvetica Physica Acta

NEW TEST FACILITY FOR SOLAR WIND INSTRUMENTATION

P. WURZ, A. MARTI, AND P. BOCHSLER
Physikalisches Institut, Universität Bern, Sidlerstr. 5, CH-3012 Bern, Switzerland

First experimental results from our new test facility for solar wind plasma particle instrumentation are presented. The test facility consists of an electron-cyclotron resonance ion source operating at 2.45 GHz using permanent magnets and an accompanying ion-optical system for ion beam analysis, definition, and delivery. Ion beams can be produced from elements in gaseous as well as solid form. A simple model to explain the observed ion charge state distributions is also introduced.

For the development, testing, and calibration of solar wind plasma instruments, test facilities providing highly charged ions beams for all elements from hydrogen up to iron are needed. Although ion sources for the desired ions have been available for some time [1, 2], the special demands of space instrumentation made it necessary to build a dedicated facility in house, which also alleviates many logistic problems encountered during calibration campaigns.

We built an electron-cyclotron resonance (ECR) ion source operating at 2.45 GHz using only permanent magnets [3]. The design of this ion source was based on an earlier design from the University of Giessen [4], which we adapted for our needs. We also added a high temperature furnace closely attached to the ion source at the location where the plasma is burning. Ions can be produced from elements in gaseous and solid phase. The latter are formed from vapor released from the high temperature furnace and introduced into an auxiliary plasma (H_2 or He). With furnace temperatures up to 2000°C all elements observed in the solar wind can be provided by this facility. Ions are extracted from the ECR ion source by a mechanically adjustable extraction electrode system to optimize the electric field for ion extraction for the particular m/q of the ion of interest in the space charge limited region of the initial ion acceleration. The ion optical system comprises an Einzel lens, a set of deflection plates, a Wien-filter, a 180° hemispherical energy analyzer, a second Einzel lens and a drift tube before the ions exit through the exit aperture (see Figure 2). The ECR ion source with the accompanying ion optical elements are installed on a high-voltage platform allowing for post-acceleration potentials of up to 100 kV. The post-acceleration is applied after the exit aperture, across the high-voltage isolator, and then the ions enter into the main chamber toward the instrument to be tested. Further experimental details of this new facility are given in [3, 5].

So far, beams of highly charged ions have been produced from various gaseous elements

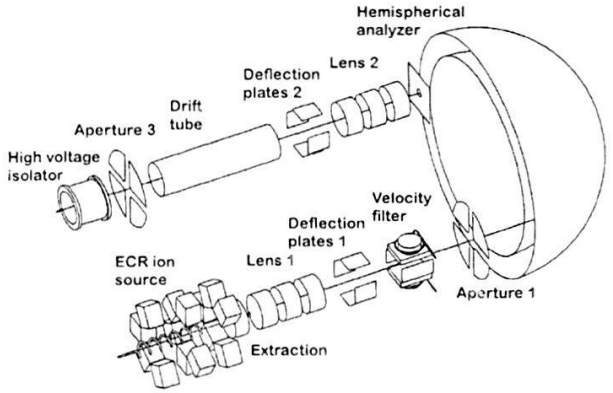

Figure 1: Schematics of the ECR ion source and the ion optical system of the new facility.

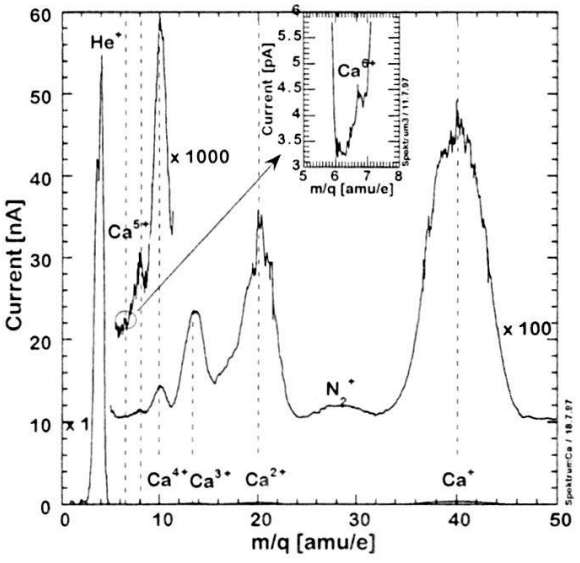

Figure 2: Charge state spectrum of a Ca ion beam. Ca was added to the auxilary He plasma through an atomic beam emitted from a high temperature oven. The ion source parameters were optimized for higher Ca charge states.

and from a few solid elements. As an example of an ion beam produced from a metallic element we show in Figure 2 the recorded charge state spectrum for a calcium ion beam. The dominating ion in the charge spectrum is the He^+ from the auxiliary discharge necessary to maintain a plasma when the element to be ionized is furnished from the high temperature furnace. The oven was kept at 475°C, which gives a Ca vapor pressure of about $1.6\ 10^{-4}$ mbar. The Ca^+ ion (at $m/q = 40$) is about a factor of 100 less intense than the He^+ ion in the ion beam. We can also identify the higher charge states of calcium Ca^{2+}, Ca^{3+}, ... Ca^{6+} at the m/q values 20, 13.3, 10, 8, and 6.7 in the ion beam. At the highest observed charge state for this run, Ca^{6+}, the ion current was still 0.5 pA, which is more than is required for the calibration of solar wind instruments.

In order to understand and predict the formation of multiply and highly ionized elements in the plasma of our ECR source, we devised a simple model consisting of a set of rate equations,

$$\frac{d}{dt}N_0(t) = N_e\left\{-N_0(t)C_0 + N_1(t)R_1\right\}$$

$$\vdots$$

$$\frac{d}{dt}N_i(t) = N_e\left\{N_{i-1}(t)C_{i-1} - N_i(t)\left(C_i + R_i\right) + N_{i+1}(t)R_{i+1}\right\}$$

$$\vdots$$

$$\frac{d}{dt}N_8(t) = N_e\left\{N_7(t)C_7 - N_8(t)R_8\right\}$$

where N_i denotes the ion density of an element in charge state i, N_e denotes the electron density, and C_i and R_i are the ionization and recombination constants for an element in the ionization state i in an electron gas of the temperature T_e, i.e. $C_i = C_i(T_e)$ and $R_i = R_i(T_e)$ [6]. Our model relies on the facts that the formation of multiply charged ions is a step-by-step process, and the actual ionization process is electron impact ionization. To obtain the ion densities N_i we integrated the set of rate equations over time, with the upper integration limit being the confinement time τ_C of the ion in the magnetic bottle of the ion source. The integration was performed for several sets of the parameters N_e, T_e, and τ_C in order to best reproduce the measured data, assuming a degree

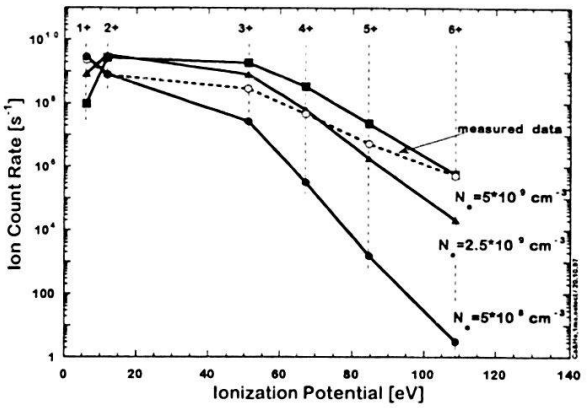

Figure 3: Calculated charge distribution for Ca ions in an ECR plasma for three electron densities and an electron temperature of 100 eV.

of ionization in the plasma of 10%. The best agreement with the measured data is found for an electron temperature T_e = 100 eV, an electron density $N_e = 5 \cdot 10^9$ cm^{-3} and a confinement time τ_C = 1 ms. Figure 3 shows three results of the calculations for Ca together with the measured charge state distribution. The agreement between our model and the measured data is reasonably good given the simplicity of our model. Also, charge state fractionation will occur in the ion optical system, and the measured charge state distributions is probably different from the charge state distribution in the plasma.

The authors are grateful to J. Fischer, H. Hofstetter, and R. Liniger, from the University of Bern, for their contributions in the areas of design, fabrication, and electronics, respectively, and to E. Salzborn, R. Trassl, and M. Liehr from the University of Giessen, Germany. The work is supported by the Swiss National Science Foundation.

[1] R. Geller and B. Jacquot, Nucl. Instr. Meth. 184, 293–296 (1981).
[2] F. Bourg, R. Geller, and B. Jacquot, Nucl. Instr. Meth. A254, 13–21 (1987).
[3] A. Marti, PhD Thesis, University of Bern, Switzerland (1997).
[4] M. Liehr, R. Trassl, M. Schlapp, and E. Salzborn, Rev. Sci. Instr. 63, 2541–2543 (1992).
[5] A. Marti, P. Wurz, and P. Bochsler, Rev. Sci. Instr., to be submitted (1998).
[6] M. Arnaud and R. Rothenflug, Astron. Astrophys. Suppl. Ser. 60, 425–457 (1985).

Helv. Phys. Acta 71, Separanda 1 (1998) S25 – S26
0018-0238/98/0100S25-02 $ 1.50+0.20/0

Helvetica Physica Acta

Stellar Mass Loss - A Central Problem in Astrophysics

W. Schmutz

Institute of Astronomy, ETH Zentrum, CH-8092 Zürich, Switzerland

Mass loss is of central importance for the theory of stellar evolution which in turn, has as one of its most important applications the understanding of the metallicity evolution in galaxies and in the universe. It is emphasized that mass loss is not yet sufficiently well understood that a save extrapolation to the low metallicity case, i.e. the early universe, can be made. Especially, the dependence on the stellar parameters of the mass loss in the Wolf-Rayet phase, which is important for the enrichment of light elements such as C and N, is extremely uncertain.

How does the metal abundance of a galaxy evolve as a function of time? Clearly the metallicity evolution of a galaxy is directly tied to the evolution of its stellar components. Stars produce new elements and deliver them to the interstellar medium. Each new generation of stars continues the process starting from matter that has been previously enriched in metals. This simple picture becomes much more complicated when the details are investigated. It is one of the important applications of stellar evolution theory to evaluate the stellar yields as a function of the initial mass and metallicity.

Maeder [1] has found that the stellar yields have a strong dependence on metallicity. This result is a consequence of the mass loss properties of the stars: the stellar yields are different when a star ejects some of the newly produced elements, like nitrogen, via a stellar wind (strong stellar winds are thought to be a consequence of high metallicity) or when these elements are only intermediate products that would be processed further in the interior of a star that does not lose mass (weak stellar winds are predicted for low metallicity). For instance, nitrogen is destroyed before the stellar envelope is ejected in a supernova event.

It is therefore clear that the predictions of stellar evolution depend crucially on the properties of stellar winds as a function of stellar parameters and the initial metallicity of the stellar material. The important question to ask at this point is whether stellar winds are sufficiently understood for a reliable prediction. The answer is no.

The reason for this negative answer is that the important phases for metal enrichment are the early phases of galaxy evolution at low metallicity. However, we cannot observe the massive stars of these epochs because in our vicinity they are long gone and in remote galaxies we cannot observe single stars. Thus, there is no empirical calibrations for the properties of stars with an extreme low metal abundance and for the calculations of the stellar yields we have to rely completely on theoretical predictions. The only way we can verify the theoretical wind predictions is to compare them with observed properties of stars in the range of 1/10 to solar metallicity. Even small discrepancies between observed and predicted values have to be taken seriously because we use the theory to extrapolate to the extreme low metallicity case.

It is commonly accepted that the radiation pressure creates mass loss during the early phases of massive stars [2]. Qualitatively, radiation-hydrodynamic calculations reproduce the observed dependence of mass loss rates on the stellar parameters. However, quantitative predictions compare less favorably with observational results. It has been pointed out [3, 4, 5] that there are small but real systematic discrepancies between the observed wind properties of galactic O stars and the predictions by hydrodynamical calculations.

There is one especially productive evolutionary phase that is responsible for the enrichment of the interstellar medium by light metals such as carbon and nitrogen. This is the Wolf-Rayet (WR) phase which is the last stage of massive stars before they explode as supernovae. During this phase WR stars have a very strong mass loss of highly non-solar composition of the matter. The origin of the the strong mass loss of the WR stars is not known and therefore, in order to treat these phases, the theory of stellar evolution has to resort to highly uncertain relations between stellar parameters and mass loss rates.

A theoretical understanding of mass loss in the WR phase is urgently needed. There is also a hope that if we understand what drives the WR winds, then the remaining discrepancy of the predicted O star winds will also be removed. It is suspected that the radiation field is responsible for driving the wind in WR stars as is the case for the O stars. However, up to now it has not been possible to prove this hypothesis. The WR phase is characterized by very high mass loss rates that deviate clearly from the luminosity - mass loss relation that holds for O stars. Many researchers believe that this deviation is a strong indication that a yet unknown mechanism is operating in the WR phase [6].

For more than two decades researchers have been trying to determine the origin of the mass loss of WR stars [7, 8, 9]. Recently, it has been possible to calculate a hydrodynamical solution for the wind's acceleration in the optically thin part of the atmosphere [10]. This solution is an important step towards understanding WR winds. For the first time, the hydrodynamic solution has been consistently coupled with the modeling of the observed line strengths and profiles. The problem of the mass loss of WR stars now splits into two parts: first, the creation of the mass loss and the acceleration to a photospheric expansion velocity within the optically thick part of the stellar atmosphere. Then second, there is a further acceleration in the observable, optically thin part from the photospheric to the terminal velocity of the wind. The second part can be modeled successfully with hydrodynamic calculations based on the radiation pressure, whereas the first part is not yet understood. With this new result it has been established that at least the acceleration of the outer WR wind is due to the radiation pressure.

References

[1] Maeder A., A&A **264**, 105 (1992)
[2] Kudritzki R.P., Hummer D.G., ARA&A **28**, 303 (1990).
[3] Lamers H.J.G.L.M., Leitherer C., ApJ **412**, 771 (1993)
[4] Schaerer D., Schmutz W., A&A **288**, 231 (1994)
[5] Kudritzki R.P., et al., In "Second Boulder Munich workshop", in press (1998)
[6] Cassinelli J.P., IAU Symp. **143**, 289 (1991)
[7] Cassinelli J.P., Castor J.I., ApJ **179**, 189 (1973)
[8] Pauldrach A., Puls J., Hummer D.G., Kudritzki R.P., A&A **148**, L1 (1985)
[9] Lucy L., Abbott D.C., ApJ **405**, 738 (1993)
[10] Schmutz W., A&A **321**, 268 (1997)

Helv. Phys. Acta 71, Separanda 1 (1998) S27 – S28
0018-0238/98/0100S27-02 $ 1.50+0.20/0

Helvetica Physica Acta

Radiative Shocks and Structure Formation in Space

Rolf Walder[1] and Doris Folini[1,2]

[1] Institut für Astronomie, [2] Seminar für Angewandte Mathematik, ETH Zürich

In combination with radiative cooling, (magneto-)hydrodynamical instabilities in shocked flows strongly contribute to structure formation on scales ranging from dense clumps in stellar atmospheres, over planetary knots in wind driven structures, to the formation of stars and galaxies. On a time scale on the order of a flow cooling time, supersonic turbulence is excited in the collision zone between the flows, and high density knots and filaments are formed. Possible observable consequences range from strongly broadened emission lines to enhanced X-ray emission.

In space radiative shocks play an outstanding role. They not only emit most of the light (except for stars), they also significantly contribute to structure formation. Radiative shocks are generally unstable, which leds to the formation of highly compressed condensates in the form of knots and filaments. In this way, they have an impact on the structure and the dynamics of the interstellar medium, the shape of supernovae remnants (SNR) and large ring-nebulae, or the fragmentation of dark clouds. They possibly trigger the birth of stars [1] and may contribute to galaxy formation. However, the physics of radiative shocks is not yet well understood. A better understanding of the turbulent shock solutions relevant for astrophysical colliding flows will have a strong impact on the understanding of structure formation in space as well as on the radiative emission from shocks in all wavelengths.

Astrophysical flows are generally magnetic and self-gravitating. In radiative shocks radiative transfer, ionization, dissociation, and similar processes are important. Such highly non-linear systems generally cannot be solved analytical and one has to take rescue to numerical solutions. However, even significantly increased computer power would not allow to simulate flows in the generality sketched above in three space dimensions. The results we present, although restricted to Euler flows in two space dimension and parameterized radiative cooling, are already on the edge of feasibility. Graphical representation of the computed flows by video sequences is a valuable tool for analyzing the numerical output. [2].

When two hypersonic flows collide, the interaction zone is bounded by two strong shock waves. Fig. 1 shows the numerical simulations of two different cases: The asymmetric case, where only one shock is radiative while the other one is nearly adiabatic, and the symmetric case, where both shocks are radiative. Within a cooling time, the shocks become unstable and excite a supersonically turbulent flow in the interaction zone. Under the ram-pressure of the two flows, the already cooled matter gets compressed by M^2, where M is the Mach-number. In SNRs or hot star winds M^2 easily reaches 10'000 or more. The supersonic turbulence leads to a complex density and velocity distribution. Cells of overcompressed matter eventually form which may reach the Jeans limit and collapse gravitationally.

In the asymmetric case (Fig. 1, left), the turbulence is driven by Rayleigh-Taylor (RT) and Richtmyer-Meshkov (RM) instabilities which, themselves, are triggered by the thermal cooling instability [3]. The resulting structure consists of three layers. - The thermally

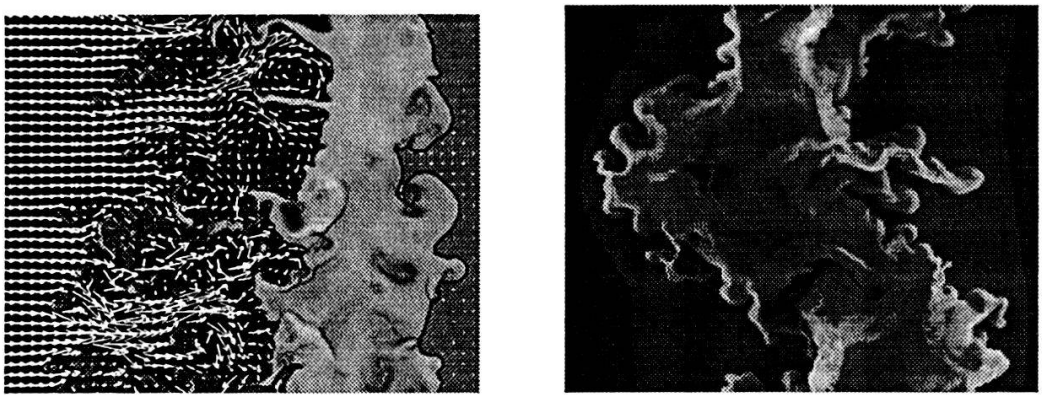

Figure 1: The turbulent interaction region of colliding hypersonic radiative flows shown in density (black corresponding to low, white to high density) and the velocity field. Left panel: asymmetric case, right panel: symmetric case.

unstable cooling layer of the shock (right). - A layer of extremely compressed cold gas (middle) Mildly supersonic turbulence diversifies the density and velocity in the layer. RT and RM spikes grow because the confining interfaces are accelerated by the thermally unstable shock. - A classical, Kelvin-Helmholtz (KH) excited, turbulent mixing layer (left side), where shocked hot gas streams subsonically around broken off condensates, ablating cold material, and causing efficient X-ray emission.

In the symmetric case, (Fig. 1, right), the turbulence is mostly driven by unbalanced momentum transport in the thin layer (middle) of compressed gas confined by the ram-pressure of the flows ([4], [5]). By exciting RT, RM and KH instabilities the flows in the two cooling layers (left and right) significantly enhance the turbulence. The turbulence in the cold layer is extremely supersonic (up to Mach 10). A cellular pattern of high density walls and nearly evacuated cells forms. Supersonic flow is embedded in extremely subsonic patches. Although unsteady, these patterns have a long lifetime and form coherent structures in the turbulent gas. Energy is dissipated by strong shocks rather than by a vorticity cascade. Occasionally, violent eruptions occur driving the turbulent layer against the accretion shocks.

We conclude that structure is efficiently generated in radiative colliding hypersonic flows on a time scale on the order of the cooling time. The condensates can have densities corresponding to a compression rate of up to ten times the Machnumber squared of the flows. Presumably, the condensates have no unique length scale.

References

[1] J. H. Hunter, Jr., M. T. Sandford II, R. W. Whitaker, and R. I. Klein. Star formation in colliding gas flows. *ApJ*, 305:309–332, 1986.

[2] R. Walder, D. Folini, and J. Favre. Stability of colliding radiative flows, 1997. Video animations, http://www.astro.phys.ethz.ch/staff/walder/.

[3] R. Walder and D. Folini. Knots, filaments, and turbulence in radiative shocks. *A&A*, 330:L21–L23, 1998.

[4] E. T. Vishniac. Nonlinear instabilites in shock-bounded slabs. *ApJ*, 428:186–208, 1994.

[5] J. M. Blondin and Brian S. Marks. Evolution of cold shock-bounded slabs. *New Astronomy*, 1:235–244, 1996.

Helv. Phys. Acta 71, Separanda 1 (1998) S29 – S30
0018-0238/98/0100S29-02 $ 1.50+0.20/0

Helvetica Physica Acta

VOM WASSERSTOFFATOM ZUM UNIVERSUM

E. MUFF, Wiberg 4, St. Erhard

The radius and energy of the hydrogen atom in the case of a variable velocity of light c(t) in a background are calculated. The unities of length and proper time are dependent on these quantities. The same is explained with light clocks. In cosmology c(t) can be determined and gives the red shift of fixed galaxies but variable c(t) in terms of the Hubble-constant. A scalar field equation for gravitation and a metric field equation for motion are distinguished.

Für verschiedene Grundgrössen als Funktion der Lichtgeschwindigkeit wird der folgende Fall eingehender betrachtet. Der Radius und die Energie des Wasserstoffatomes $r\sim \varepsilon_o/m$ und $E\sim m/\varepsilon_o^{\,2}$ werden bei zeitlich veränderlicher Lichtgeschwindigkeit c(t) für den Hintergrund berechnet. Mit der konstanten Vordergrundgeschwindigkeit c sei $k(t) = c(t)/c$. Analog sei bei ortsabhängiger Lichtgeschwindigkeit $k(x) = c(x)/c$. Bei konstanter Energie $E=mc^2\sim 1$ folgen $m\sim 1/k^2$ und mit $v\sim k$ für den Impuls $p=mv\sim 1/k$. Beachtet man $1/c^2= \varepsilon_o\mu_o$, so wird $\varepsilon_o\sim 1/k$, daher ist $r\sim k$. Mit $E\sim 1$ ist die Frequenz $\upsilon\sim 1$, d.h. es gelten dieselben Eigenzeiten für eine Periode. Bei konstantem Impuls hingegen $p=mv\sim 1$ folgen $m\sim 1/k$ und $r\sim 1$ sowie $E\sim k$, d.h. verschiedene Eigenzeiten. Dies wird aus Lichtuhren in einem Gravitationsfeld ersichtlich. Die Lichtuhr A auf höherem Potential sende Lichtwellen an die Lichtuhr B auf tieferem Potential. Die Anzahl Perioden, die in B ankommen bleibt unverändert. Die Lichtquanten haben auf dem Wege von A nach B hingegen Energie gewonnen und zeigen demnach in B eine höhere Frequenz. Dies ist nur möglich, falls die Lichtuhr in B um den Faktor $k\sim c(x)/c$ langsamer geht, d.h. die Eigenzeit wird neu definiert. Die Lichtgeschwindigkeit in B gemessen mit der dortigen Eigenzeit ist aber wieder das konstante c. Die Länge der Lichtuhr verändert sich bei einer weiteren Geschwindigkeit $c^*(x)$ um den Faktor $k^*\sim c^*(x)/c$ gemessen in der dortigen Eigenzeit. Die Funktionen k bzw. k^* sind mit der Metrik g^{ij} über g^{oo} bzw. über den Anteil der Längenmetrik verbunden. Die Länge der Lichtuhr ist daher $l\sim r\sim 1/k^*$ oder als Resonator proportional zur Wellenlänge $\lambda\sim 1/p$. Die Hintergrundgeschwindigkeit gemessen in der Koordinatenzeit ist dann proportional zu $k\cdot k^*$. Wegen der Symmetrie zwischen Zeit und Raum als Radius bei Kugelsymmetrie ist $k^*=k$.

Im Falle der Kosmologie wird die Funktion c(t) aus folgenden Überlegungen berechnet. Die Metrik aus dem Hintergrund (x_o, x) nach Minkowski sei $\gamma^{\alpha\beta}$ und die Metrik aus dem Vordergrund $(t, x/k)$ nach Riemann g^{ij}. D_α sei die kovariante Ableitung bezüglich der Hintergrundmetrik. Mit der kovarianten Zeit $x_o= \int^t_o c(t)dt$ folgt bei global gleich laufender Eigenzeit $g^{oo}\sim 1/c^2(t)$. Es gelte die Feldgleichung

$$\gamma^{\alpha\beta}\, D_\alpha\, D_\beta\, g^{ij} = \kappa\, T^{ij} \quad (1) \quad (\kappa = Gc^{-4} \sim k^5\cdot k^{-4}).$$

Dabei ist die Gravitationskonstante in der Hintergrundmetrik $G\sim k^5$ und folgt analog wie beim Wasserstoffatom, wobei die Coulombkraft durch die Gravitationskraft zu ersetzten ist mit $r\sim k$. Im Vordergrund hingegen ist $G\sim k^2$.

Im Fall g^{oo} erhält man hieraus bei konstanter Energiedichte des Vordergrundes $\varepsilon\sim 1$ die Lösung $c(t) \sim \varepsilon^{-1/4}\cdot t^{-1/2}$.

Die Beziehung für Lichtwellen $\lambda\cdot\upsilon \sim k(t)$ gilt für den Beobachtungsort B zum Zeitpunkt des Alters T des Universums als auch für das beobachtete Objekt A zum Zeitpunkt t der zugehörigen Lichtemission. Da die Länge eines Wellenzuges im Hintergrund konstant bleibt, ist $\lambda_A = \lambda_B$. Damit ist zunächst $\upsilon_B/\ \upsilon_A = k_B(T)/k_A(t)$. Berechnet man die Distanz $r= \int^T_t c(t)dt$ zwischen A und B im Hintergrund, so gilt die Hubble-Beziehung

$$\upsilon_B/\ \upsilon_A = 1 - H\cdot r \quad \text{mit} \quad H^{-2} = 2\,\tau\, T\, c^2.$$

Das Ergebnis ist ein offenes Universum vom Alter T mit der Halbwertzeit τ bestimmt aus ε. Mit dem gegenwärtigen Wert von G ohne Wechselwirkung ist die Energiedichte ε

berechenbar. Aus dem Alter T des Universums kann ausserdem die Hintergrundgeschwindigkeit des Lichtes und umgekehrt bestimmt werden.

Im Falle von eingebetteten diskreten Massenpunkten verwendet man eine zu (1) analoge Feldgleichung mit einer zusätzlichen Nebenbedingung für ein neu definiertes Metrikfeld. Nämlich die Gleichung $\gamma^{\alpha\beta} D_\alpha D_\beta \tilde{\phi}^{ij} = \kappa \tilde{T}^{ij}$ mit $\tilde{\phi}^{ij} = (-g)^{1/2} g^{ij} - (-\gamma)^{1/2}\gamma^{ij}$ und $\tilde{T}^{ij} = (-g)^{1/2} T^{ij}$. Die Nebenbedingung nach Logunov ist $D_i \phi^{ij} = o$ gemäss $\tilde{\phi}^{ij} = (-\gamma)^{1/2}\phi^{ij}$. Dabei ist G durch $G_m = 3G$ mit Wechselwirkung zu ersetzen, da die kosmologische Lösung ebenfalls diese Feldgleichung erfüllen soll. Aus dem gemessenen G_m folgt $G=G_m/3$ und damit ist im Vordergrund die Energiedichte $\varepsilon = 6c^4H^2/G_m$. Durch die Nebenbedingung wird gleichfalls die kosmologische Lösung physikalisch eindeutig. Das Metrikfeld bildet die Grundlage der Bewegungsgleichung und ist verschieden vom Gravitationsfeld. Für das skalare Gravitationsfeld ϕ mit der Massendichte ρ wird $\gamma^{\alpha\beta} D_\alpha D_\beta \phi = G\rho$ als Feldgleichung verwendet. Die zugehörige negative Feldenergie ist im Energie-Impulstensor T^{ij} zu berücksichtigen. Mit der negativen Feldenergie der Gravitation kann die Singularität von Schwarzschild behoben werden.

Literatur aus dem Eigenverlag seit 1975:

1. Vom Wasserstoffatom zum Universum.
2. Geometrie und Elektrodynamik.
3. Quantum Theory und Gravity.
4. Aethersubstrat und Relativitätstheorie.
5. Periheldrehung und Lichtablenkung vor der Relativitätstheorie.
6. Eine neue Möglichkeit das Weltall zu besiedeln.